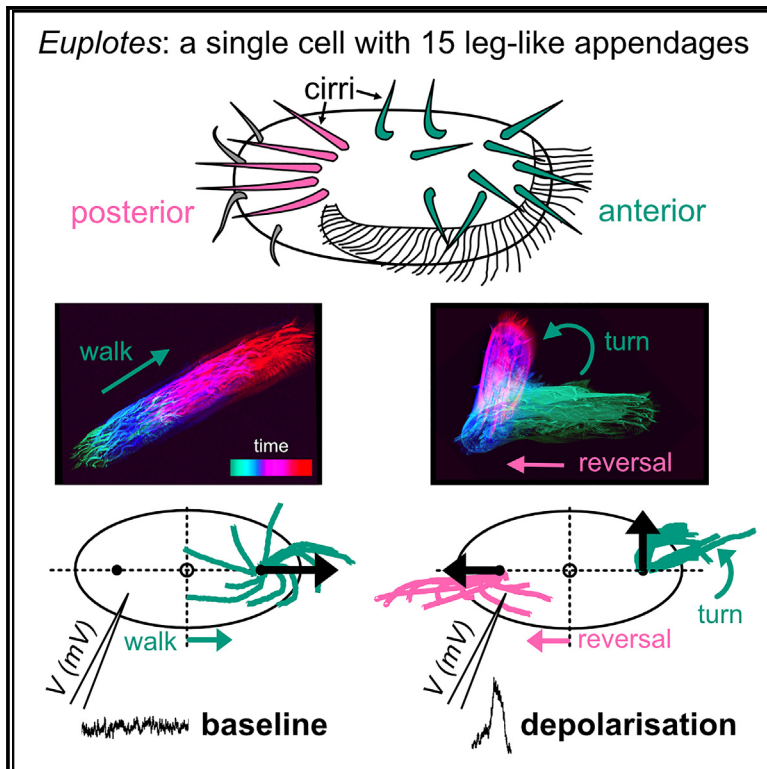# Bioelectric control of locomotor gaits in the walking ciliate *Euplotes*

Graphical abstract

Authors

Hannah Laeverenz-Schlogelhofer,
Kirsty Y. Wan

Correspondence

h.laeverenz-schlogelhofer@exeter.ac.uk
(H.L.-S.),
k.y.wan2@exeter.ac.uk (K.Y.W.)

In brief

Laeverenz-Schlogelhofer et al. combine high-speed imaging with simultaneous electrophysiological recordings in *Euplotes*, a single cell with leg-like appendages (cirri), to show how the cell's membrane potential coordinates cirri movement and dynamic transitions between whole-cell walking or turning.

Highlights

- *Euplotes* uses bundles of cilia (cirri) on its ventral surface to walk and swim

- Forward movement is interrupted by highly coordinated turning maneuvers

- Membrane depolarizations trigger turning with distinct cirri behaving differently

- A minimal mechanical model maps cirri dynamics to locomotor gait

CellPress

Article

Bioelectric control of locomotor gaits in the walking ciliate *Euplotes*

Hannah Laeverenz-Schlogelhofer[1,2,*] and Kirsty Y. Wan[1,3,4,*]
[1]Living Systems Institute, University of Exeter, Stocker Road, Exeter EX4 4QD, UK
[2]X (formerly Twitter): @hannahscope
[3]X (formerly Twitter): @micromotility
[4]Lead contact
*Correspondence: h.laeverenz-schlogelhofer@exeter.ac.uk (H.L.-S.), k.y.wan2@exeter.ac.uk (K.Y.W.)
https://doi.org/10.1016/j.cub.2023.12.051

SUMMARY

Diverse animal species exhibit highly stereotyped behavioral actions and locomotor sequences as they explore their natural environments. In many such cases, the neural basis of behavior is well established, where dedicated neural circuitry contributes to the initiation and regulation of certain response sequences. At the microscopic scale, single-celled eukaryotes (protists) also exhibit remarkably complex behaviors and yet are completely devoid of nervous systems. Here, to address the question of how single cells control behavior, we study locomotor patterning in the exemplary hypotrich ciliate *Euplotes*, a highly polarized cell, which actuates a large number of leg-like appendages called cirri (each a bundle of ~25–50 cilia) to swim in fluids or walk on surfaces. As it navigates its surroundings, a walking *Euplotes* cell is routinely observed to perform side-stepping reactions, one of the most sophisticated maneuvers ever observed in a single-celled organism. These are spontaneous and stereotyped reorientation events involving a transient and fast backward motion followed by a turn. Combining high-speed imaging with simultaneous time-resolved electrophysiological recordings, we show that this complex coordinated motion sequence is tightly regulated by rapid membrane depolarization events, which orchestrate the activity of different cirri on the cell. Using machine learning and computer vision methods, we map detailed measurements of cirri dynamics to the cell's membrane bioelectrical activity, revealing a differential response in the front and back cirri. We integrate these measurements with a minimal model to understand how *Euplotes*—a unicellular organism—manipulates its membrane potential to achieve real-time control over its motor apparatus.

INTRODUCTION

A major focus of modern neuroscience is to understand the biological mechanisms that underlie the behavior of living systems. The neural and genetic basis of behavior in diverse species, including flies, worms, and mice, have been elucidated by interrogating how internal signaling relates to physiological or ethological data obtained from behaving organisms.[1–3] The ability to control and coordinate movement is a fundamental feature of life, which allows individuals to explore their surroundings, locate more favorable habitats and avoid harmful situations. Even the most basic unit of life, a single cell, displays these abilities in abundance.[4,5] This has profound implications for the evolution of sensorimotor coupling, environmental perception, and basal cognition across phyla.[6] Notable examples include animal-like feeding,[7] hunting,[8] predation,[9] and mating behaviors of free-living protists,[10] as well as associative learning in the "trumpet animalcule" *Stentor*.[11–13]

How are complex behavioral actions encoded within the confines of a microscopic body? Essential clues lie in the movement of diverse microbes. The ciliate *Paramecium* swims using distinct gaits,[14,15] described by Jennings as "its action system—the characteristic set of movements by which its behavior under all sorts of conditions is brought about."[16] *Escherichia coli* exhibits run-and-tumble motility, comprising straight runs when the flagellar bundle is synchronized and stochastic tumbles when the bundle splits apart.[17,18] The marine alga *Pyramimonas octopus* adopts a run-stop-shock strategy using eight cilia, switching between forward and fast backward swimming.[19,20] The freshwater alga *Chlamydomonas reinhardtii* swims using a eukaryotic run-and-tumble, where ciliary coordination again dictates the gait.[21] Microorganismal movement can thus be coarse-grained into a small set of locomotor states, with fast and slow episodes. By flexibly combining different gaits, single cells perform complex maneuvers.[22–24] This is analogous to how animals chain together modular, stereotyped movements into more complex sequences, or "bouts," to achieve specific goal-directed behaviors.[25–27]

How do protists control whole-body movements if they cannot rely on animal-like central pattern generators?[28,29] Various conjectures have been proposed for ciliates—a major class of organisms for studying how cells coordinate appendages. Ciliates are distinguished by their large size, complex morphology, and exotic arrangements of cilia on a highly polarized cell.[30,31] From algal flagellates to ciliates, intricate structures extending between or in association with basal bodies are involved in the mechanical

coordination of cilia motility.[32–35] Dynamic contraction of the basal apparatus and/or cytoskeleton implicates a putative *ciliary neuromotor apparatus*.[36,37] Ciliate behavior can also change rapidly when responding to cues, reminiscent of bioelectrical signaling from sensor to effector.

Since Hodgkin and Huxley's seminal demonstration of action potentials propagating across excitable cells,[38] bioelectrical activity has been shown to be responsible for surprisingly diverse functions.[39,40] This includes the wound response of plants,[41,42] migration of epithelial cells in animals,[43,44] to the germination transition of bacterial spores,[45] and bioelectric communication across bacterial biofilms.[46,47] In ciliates, pioneering studies used sharp-electrode recordings to measure membrane potential and ion channel conductances.[48,49] These produced detailed measurements of cellular responses to different stimuli (e.g., intracellular current injection, chemical cues, or mechanical stimulation),[50–54] sometimes coupled with behavioral quantification.[55–57] Together, these studies have led to the emerging perspective that ciliate motility may be under bioelectric control.

In this work, we explore how bioelectrical signaling controls whole-cell behavior and locomotor patterning in *Euplotes*, a ciliate widely distributed in freshwater and marine environments.[58] These organisms are among the most morphologically complex and differentiated groups of ciliates. Each cell has a characteristic number of cirri (compound leg-like structures comprising many cilia), which it actuates in distinct patterns to swim or walk across surfaces[10,34] (Figure 1). Cells have a modular gait, locomotion is spontaneously interrupted by stops or sharp turns.[59] Previous work in other ciliated organisms already suggested a correlation between intracellular membrane potential, cilia dynamics, and locomotion gait. In the densely ciliated *Paramecium*, voltage-gated Ca^{2+} channels elicit ciliary reversal and backward swimming upon membrane depolarization,[14,48] which is also observed in the biciliated *Chlamydomonas*.[60,61] *Euplotes* also displays spontaneous depolarizations,[62] which can be effected by chemical cues.[63,64] The effect of membrane potential on cirral movement in such walking ciliates has been minimally characterized and is inconclusive.[62,65–69] This emphasizes the need for quantitative study and the development of an integrative perspective.

To temporally match cirri movement to the cell's membrane potential, we perform simultaneous high-speed imaging and electrophysiology (inserting the recording electrode into immobilized cells). We use machine learning and semi-automated tracking to quantify observed cirri waveforms and dynamics, revealing the functional relationship between membrane potential and cirri activity across the entire cell. We then propose a multiscale model of how membrane bioelectrical activity controls specific groups of spatially separate cirri and thus mediates *Euplotes'* modular walking gaits.

RESULTS

The complex motility patterns of *Euplotes*

We study *Euplotes vannus*, hereafter referred to as *Euplotes* (see STAR Methods). Cells have a highly complex and stereotyped architecture (Figures 1A–1C). Each *E. vannus* cell has 10 frontoventral cirri, five transverse cirri and typically four caudal cirri (primarily sensory and do not contribute to movement[37]). Each cirrus is composed of 25–50 tightly bundled cilia and protrudes

from the ventral surface of the cell (Figure 1D). Each cell also has a large membranelle (or membranellar) band of cilia,[70] which mostly contributes to feeding.[71]

Freely moving cells have diverse behaviors (Figure 1E). Trajectories are categorized as either 3D helical swimming in bulk fluid ($v_{swim} = 548 \pm 160$ μm s^{-1}, n = 339 trajectories), or a slower surface-based walking motility ($v_{walk} = 237 \pm 121$ μm s^{-1}, n = 133 trajectories) (see STAR Methods). Movement is intermittent, interrupted by periods of quiescence (Figure 1F).

Motility is predominantly generated by the frontoventral and transverse cirri (Videos S1, S2, and S3). Cirri beating freely in the fluid cause the cell to swim in helices, whereas near a solid substrate they perform a stepping-like motion, which enables the cell to walk. Distinct cirri are involved in generating distinct gaits (Figures 1G–1J). During forward walking, the frontoventral cirri typically beat with a power stroke toward the posterior. In contrast, the transverse cirri beat only irregularly and are often stationary when the cell is walking. Neither the membranelle band nor the caudal cirri significantly contribute to walking motility (fluctuations are observed in both during the stop state when the cell body is at rest, see Video S2). This is consistent with observations in other *Euplotes* species.[34,72]

Next, we focus on the walking dynamics. Single-cell trajectories have large speed fluctuations with phases where the cell stops walking completely (Figure 1G). Sudden changes in direction appear when *Euplotes* performs the *side-stepping reaction* (SSR), a sophisticated maneuver involving complex coordination of cirri (Figure 1J). SSRs occur spontaneously or as an escape response when cells are mechanically stimulated.[59,62]

Spontaneous SSRs are stereotyped (n = 155), with a fast backward motion followed by a large turn (Figure 1K). Turning is almost invariably counterclockwise (viewed from the ventral side) (Figure 1L). From high-speed videos, we observe that the backward motion is largely due to anteriorly directed beating of the transverse cirri, whereas turning is due to the sideways power stroke of the frontoventral cirri (Figure 1I; Video S3). Walking and stopping state durations are exponentially distributed, but duration of SSR events is peaked, with a mean of 0.3 s (Figures 1M–1O). The approximate state probabilities (i.e., fraction of time spent in each state) were stop = 0.33, walk = 0.63, and SSR = 0.04. Thus, the active walking of *Euplotes* has a discrete structure comprising episodes of quiescence, persistent forward walking, and transient but stereotyped SSR events.

Actively walking cells have a bimodal membrane potential

To investigate what kind of intracellular signaling may be responsible for the distinct walking gaits, we performed electrophysiology on *Euplotes*. Membrane potential was measured by inserting an intracellular (sharp) recording electrode into single cells that were first immobilized by a second holding pipette (Figure 2A). The spontaneous (no applied stimuli) electrical activity of 15 cells were recorded, to produce 27 traces of 30–200 s in duration.

Membrane potential recordings were temporally matched to high-speed images of the cirri, for cells held in different orientations (Figures 2B–2G; Videos S4, S5, and S6). Results for three different cells, in two different orientations, are shown in Figure 2D. Cirri activity is quantified using an approximate cirrus beat frequency, from the mean pixel intensity (I_{ROI}) across a region of
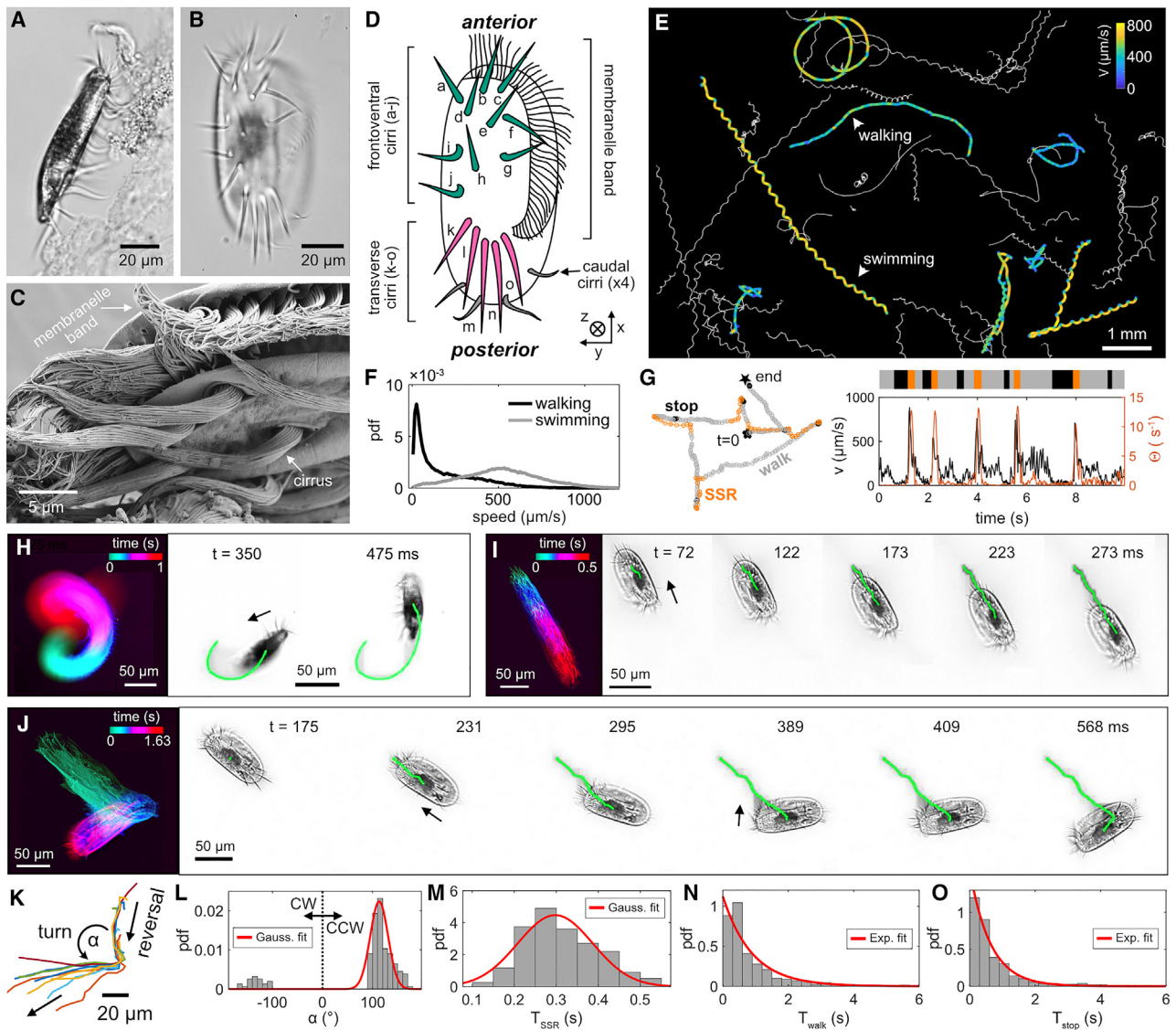
Figure 1. Body architecture and locomotor patterns of *Euplotes vannus*

(A and B) Brightfield images showing the lateral (A) and ventral (B) view of a *Euplotes vannus* cell. Average body dimensions: $L = 83 \pm 6\ \mu m$ (n = 14), $W = 39 \pm 4\ \mu m$ (n = 8), and $D = 19 \pm 3\ \mu m$ (n = 6).

(C) SEM image of *Euplotes vannus* showing its intricate and complex architecture, including the densely ciliated membranelle band and bundles of cilia that form individual cirri.

(D) Schematic of a *Euplotes vannus* cell showing the arrangement of its 15 cirri that protrude from the ventral surface, with 10 frontoventral cirri (A–J) and 5 transverse cirri (K–O).

(E) Trajectories of swimming and walking cells with example tracks color coded according to speed. Arrows point to example tracks.

(F) Histograms of cell migration speed computed separately for swimming (n = 339) and walking (n = 133) walking trajectories.

(G) Example trajectory of a walking cell color coded according to its three possible motility states: stop, forward walking, and the side-stepping reaction (SSR), alongside the corresponding time series of cell speed $v(t)$ and the orientation parameter $\Theta(t)$.

(H–J) Composite images, color coded by time, and time-lapse of body and cirri dynamics during helical swimming (H), forward walking (I), and the SSR (J) (Videos S1, S2, and S3). (Black arrows indicate the predominant direction of the cirri power strokes.)

(K) Example trajectories from eight SSR events, overlaid by aligning the reversal direction and centering the trajectories at the peak in track angle.

(L–O) Histogram of the turning angle α (n = 155 SSRs) and Gaussian fit ($\mu = 113$, $\sigma = 18$). Distributions of SSR durations fit to a Gaussian (n = 155, $\mu = 0.30$, $\sigma = 0.09$) (M), forward walking state durations fit to an Exponential (n = 431, $\mu = 0.89$) (N), and stop state durations fit to an Exponential (n = 357, $\mu = 0.63$) (O). See also Figures S1 and S2, Table S1, and Videos S1, S2, and S3.

interest (ROI), which oscillates with the beat period. We then define a normalized beat frequency $\bar{f}$ ($0 \leq \bar{f} \leq 1$) (see STAR Methods) for comparison (Figure 2C, inset).

Cirri activity changes concomitantly with membrane potential, particularly during depolarizations (Figure 2D). The high-speed recordings and simultaneous membrane potential measurements
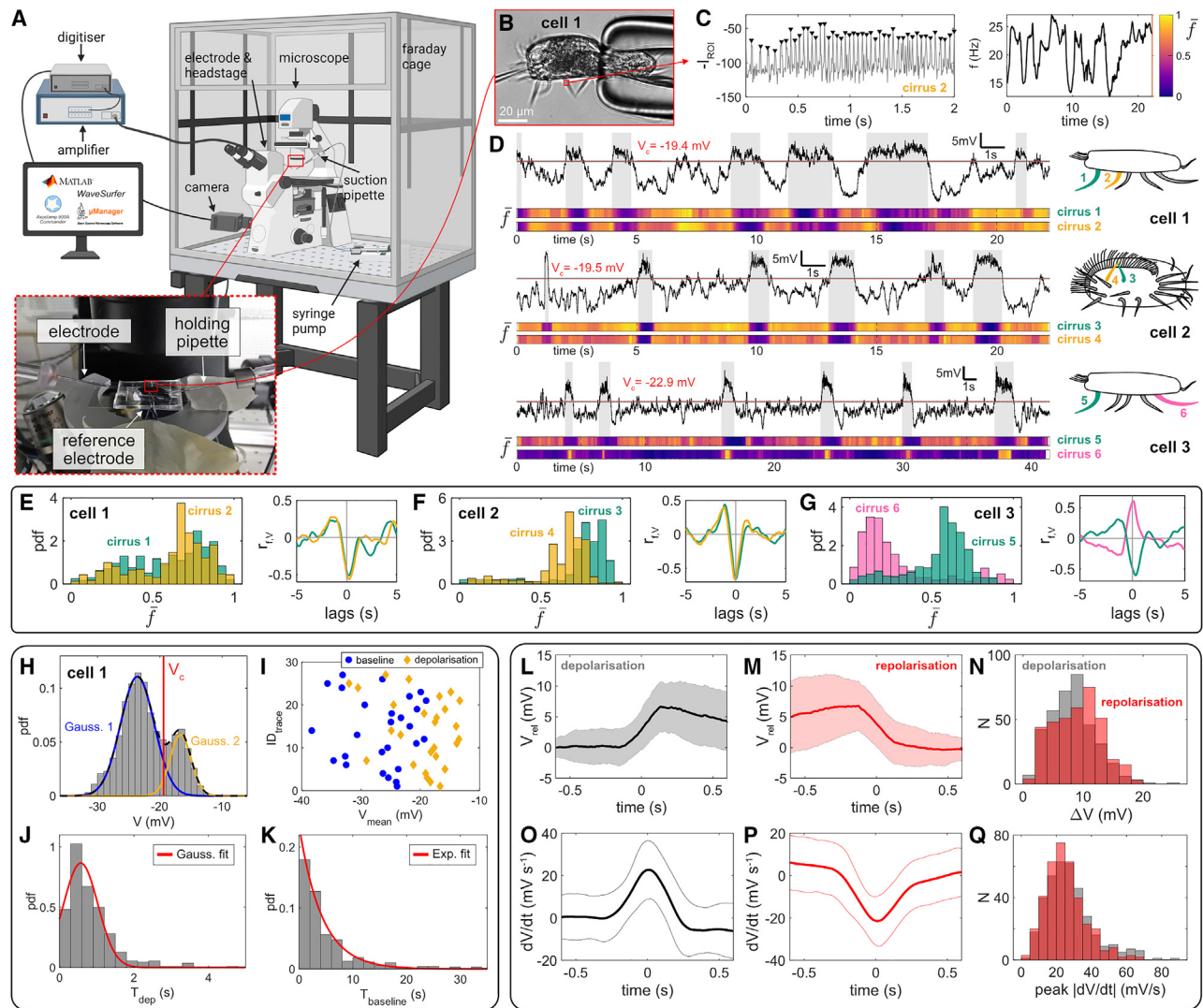
Figure 2. Simultaneous recordings of membrane potential and high-speed imaging of cirri activity

(A) Experimental setup used to measure the membrane potential of individual pipette-held cells while simultaneously recording high-speed videos.

(B) Example frame of a held-cell in lateral view.

(C) Cirri activity can be estimated by measuring mean intensity fluctuations $(-I_{ROI})$ across a pre-defined region of interest (ROI). Peaks are indicated by black triangles, from which we compute frequency f and its normalized version $\bar{f}$ (see STAR Methods).

(D) Example electrophysiology recordings for three different cells. Shading indicates depolarization events. Corresponding $\bar{f}$ time series are shown for each of the highlighted cirri.

(E–G) Distributions of $\bar{f}$ alongside the cross-correlations between $\bar{f}$ and the membrane potential V from the same recording. Note that cirri 1–5 correspond to frontoventral cirri, whereas cirrus 6 is a transverse cirrus.

(H) Membrane potential distribution for a single cell is bimodal, corresponding to two bioelectric states—baseline and depolarization events.

(I) Mean membrane potential for the baseline state (blue circles) and for depolarization events (yellow diamonds) for each of the 27 traces.

(J) Distribution of depolarization event duration, fit with a Gaussian distribution (n = 367).

(K) Distribution of baseline state duration, fit with an exponential distribution (n = 345).

(L and M) Superposition of all depolarization and repolarization dynamics (mean and standard deviation, n = 367 for depolarizations, n = 369 for repolarizations).

(N) Distributions of the magnitudes of the depolarization (step-up) and repolarization (step-down) step-sizes.

(O and P) Mean and standard deviation of dV/dt for the depolarization (O) and repolarization (P) dynamics.

(Q) Distributions of the peak in the depolarization (step-up) and repolarization (step-down) rate. See also Videos S4, S5, and S6.

(see Videos S4, S5, and S6) show that during the baseline bioelectric state, the frontoventral cirri beat regularly with a power stroke oriented toward the posterior of the cell, whereas the transverse cirri beat irregularly and are often inactive. During depolarizations, the frontoventral cirri change their waveform to point toward the anterior, whereas transverse cirri start to beat regularly with a power stroke toward the anterior of the cell. The frequency of the frontoventral cirri decreased during depolarizations, whereas for the transverse cirri the frequency increased. We also evaluated the dynamics of distinct cirri on the same cell (Figures 2E–2G).
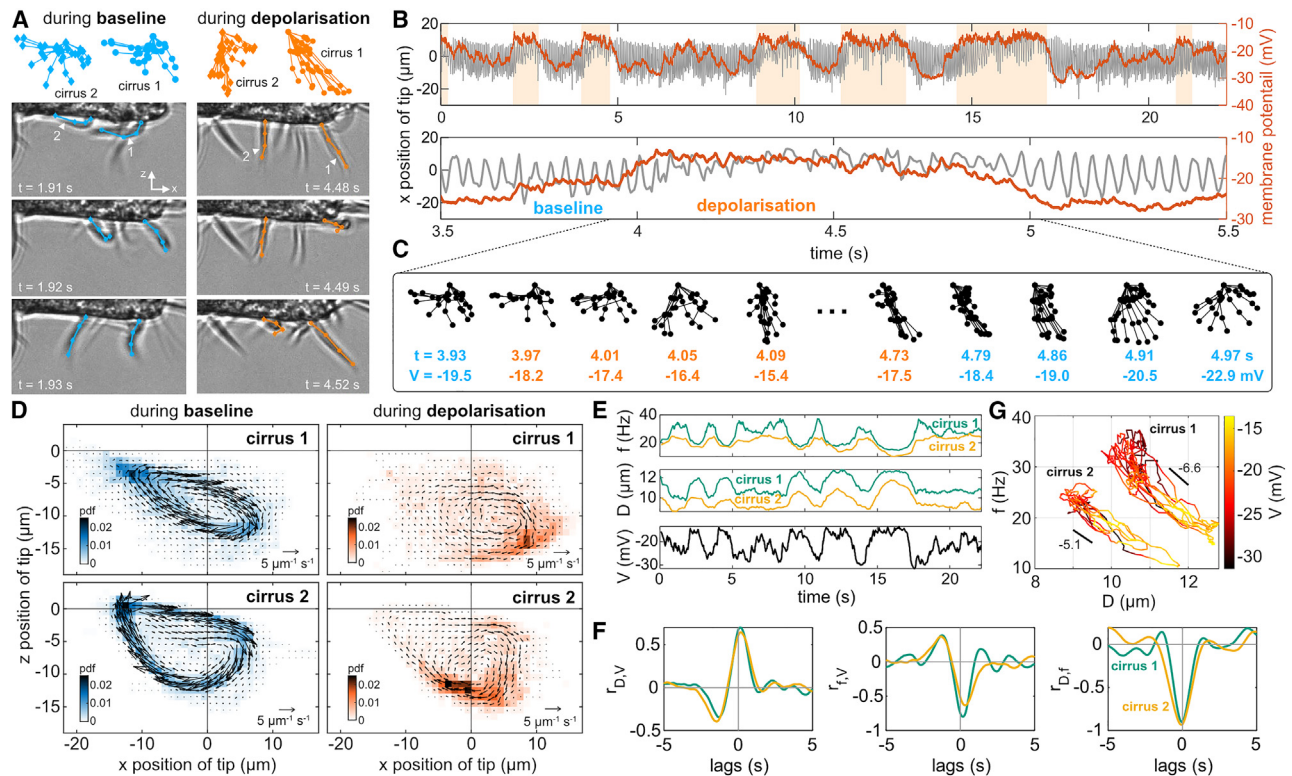
Figure 3. Membrane potential controls cirri beating

(A) Digital waveform tracking of two frontoventral cirri of a pipette-held cell (lateral view).

(B) Variation of x coordinates of the tip of cirrus 1 relative to its base, overlaid with the corresponding membrane potential trace, orange shaded regions indicate depolarization events.

(C) Tracked waveforms during a depolarization and a repolarization phases.

(D) Probability density function (pdf) for the position of the cirrus tip relative to the base overlaid with the probability flux arrows during baseline or depolarizations.

(E) Time series of cirrus beat frequency f, mean tip-to-base distance per beat cycle D, and membrane potential V.

(F) Cross-correlations of D, f, and V, for each of the two cirri.

(G) f and D mapped to the membrane potential V.

See also Video S7.

This shows that, although all the frontoventral cirri responded similarly to membrane depolarization, there is a marked divergence in the response of the transverse cirri (see later).

To establish whether membrane depolarization events are stereotyped, we binarize the electrophysiology recordings into two states: baseline (0) or depolarization (1) (see STAR Methods). For most cells, the membrane potential was bimodal, with a "baseline" or resting potential of -26 ± 5 mV (n = 27 traces, calculated using $V_{baseline}$ in Figure 2I), interspersed with depolarization events where the potential increases transiently by ~10 mV (Figures 2H, 2I, and 2N). Across all recordings, state probabilities are (0.89, 0.11) for the (baseline, depolarization) states. This is comparable to the (0.94, 0.06) we estimated previously for the probabilities that the cell is in the forward walking and SSR states, respectively, conditional on the cell being active. We did not observe the fully quiescent (stop) state in the pipette-held individuals.

Depolarizations have a mean duration of 0.57 ± 0.43 s (Gaussian fit, n = 367) and for the baseline state the expected duration was 4.3 s (exponential fit, n = 345) (Figures 2J and 2K). Defining the depolarization transition from state 0 to 1 as a *step-up*, and the subsequent repolarization from state 1 to 0 as a *step-down* response (Figures 2L–2Q), we find

that the step-up phase is associated with a change in potential $\Delta V = 8.3 \pm 3.8$ mV and peak rate $dV/dt = 28 \pm 14$ mV s^{-1} (n = 367 depolarizations), while for the step-down phase $\Delta V = -9.1 \pm 4.0$ mV and peak $dV/dt = -25 \pm 11$ mV s^{-1} (n = 369 repolarizations). Therefore, the membrane potential of a pipette-immobilized cell is bimodal. The baseline state likely corresponds to forward walking and the transient depolarization events to the SSRs routinely observed in the trajectories of freely moving cells.

Membrane potential gates cirri dynamics with a small time delay

To determine which bioelectrical state of the cell corresponds to which walking gait, we compared the membrane electrical potential measurements alongside the cirri dynamics obtained from high-speed recordings of immobilized cells. For automated cirri tracking, we implemented the machine-learning-based algorithm Social LEAP Estimates Animal Poses (SLEAP).[73] Using a skeleton of four nodes per cirrus, we tracked a 22.2 s video (imaged at 225 fps) of a cell held in the lateral (side-on) view, equivalent to ~500 consecutive beat cycles of the cirri. We post-processed and smoothed the raw coordinates of the nodes

to obtain the cirri waveforms, which we then relate to the membrane potential (Figure 3; Video S7).

We tracked two frontoventral cirri of the same cell. The cirri dynamics clearly depend on membrane potential, adopting two distinct waveforms (Figure 3A). The first is associated with the baseline bioelectric state, where the stroke patterns are typical of most cilia, with an extended power stroke toward the posterior of the cell, and a more curved recovery stroke. The second waveform sweeps over a smaller area, and the stroke asymmetry is less pronounced. Due to microscopy limitations, the extent of 3D cirri beating cannot be measured fully from 2D observations. Nonetheless, we can now relate cirri dynamics to membrane potential. Waveform changes coincide with step-up and step-down jumps in membrane potential (Figure 3B). However, the depolarization waveform only appears after the threshold membrane potential has been reached, conversely the baseline waveform is not recovered until a few beats after membrane repolarization. This suggests a latency in the cirral motor response (Figure 3C).

Cirral tip movement is another informative measure of the dynamics. We compute the spatial probability density function (pdf) of the tip positions relative to the cirrus base during the two bioelectric states, as a measure of the relative occupancy probability of the cirrus tip at each location in phase space. We then plot the associated time-averaged probability fluxes, corresponding to the most likely direction and strength of tip movement.[20,74,75] For both cirri, the tip trajectory traces out strong flux cycles during the baseline state, which reflect the strongly non-equilibrium nature of the actively beating cirri (Figure 3D). During depolarizations, the flux patterns become less ordered, consistent with the noisier beating. In this lateral projection, the beat of the frontoventral cirri also appears to be more confined toward the anterior end of the cell, with the tip tracing out a smaller area. The occupancy probability is evenly distributed along the limit cycle in the baseline state but more localized during depolarizations. The phase speed of the cirri is less uniform and can be "stuck" in certain phases of the beat cycle in the depolarization state.

To quantify how cirri beat parameters depend on the membrane potential $V(t)$, we further estimated the cirri beat amplitude $D(t)$—the mean tip-to-base distance over a given beat cycle, and beat frequency $f(t)$—inverse of the period (peak-to-peak distance in the time series of tip-to-base distance). This definition of D is akin to a stroke amplitude *transverse* to the main power stroke direction. For both cirri, V is negatively correlated with f and positively correlated with D, while f and D are anti-correlated (Figures 3E–3G). Finally, we compute cross-correlations between time series (Figure 3F). For cirrus 1, we find that D and f lags V by 0.12 and 0.17 s, respectively, whereas for cirrus 2, the lag times are 0.15 and 0.31 s, respectively. The lag times between D and V are shorter, f lags D by 0.03 and 0.07 s in the two cirri, respectively. For a typical beat frequency of $f = 20$ Hz, these lag times correspond to 1–6 beat cycles. Although the two cirri have different characteristic beat frequencies and amplitudes, they share a similar functional dependence between f and D. The activity of both cirri map similarly to membrane potential in this f-D space (Figure 3G), with the beat frequency decreasing when the beat amplitude increases.

Taken together, we have shown by simultaneous waveform tracking and electrophysiology that the cell's membrane potential

and cirri beat dynamics are tightly coupled, with V fulfilling the role of an order parameter that controls cirri beat pattern, in which f and D are enslaved to the dynamics of V with only a small time delay. These trends are consistent with results in Figure 2 and the previous section. Our long-time waveform tracking dataset is currently limited to one cell, more experiments are needed to explore the universality of these trends and whether these apply to freely walking cells (see discussion).

Forces on individual cirri can be estimated by resistive force theory

Next, to understand how changes in cirri beating impact the walking dynamics of *Euplotes*, we estimate the hydrodynamic drag on individual cirri. Given the relatively slow speed and small length-scales involved, *Euplotes* locomotion operates in a regime dominated by viscosity. Here, the Reynolds number, a key dimensionless parameter given by the ratio between inertial and viscous forces, is about 0.02, so inertial effects are negligible. Drag can be reasonably well approximated using resistive force theory (RFT), a local theory (which neglects long-range hydrodynamic interactions) that produces estimates of the forces acting on a slender filament based solely on observations of movement (Figures 4A and 4B). This method relies on accessing tracked cirri waveforms, which could not be reliably obtained by fully automated methods due to the densely overlapping cirri. Instead, we tracked cirri waveforms manually over multiple beat cycles to achieve a discretization of ∼50 points/cirrus.

For RFT analysis, we divide each filament into small segments and calculate the hydrodynamic drag force acting on each segment based on its local velocity through the fluid (Figure 4B) and then numerically integrate along the filament's length to obtain the total drag.[76,77] This approach has been applied previously to study cilia and flagella.[77–80] RFT was implemented in Python (see STAR Methods). First, cirri positions were fit to a second-order spline, to obtain curves $r(s, t)$ described by arclength $s \in [0, L]$ and time t, with a constant spacing $\Delta s = 0.4$ μm. We set the cirrus length L to be constant, equal to the mean length across all frames. For tracings shorter than L, the curve is extended using the fitted spline, while for longer tracings points for $s > L$ are discarded. Here, L was between 16 and 23 μm for the different cirri.

For each segment, the local drag force density is given by $f(s, t) = -(c_t v_t(s, t) + c_n v_n(s, t))$, where $v_t(s, t)$ and $v_n(s, t)$ are the tangential and normal components of the local velocity, respectively. The tangential and normal drag coefficients are

$$c_t = \frac{2\pi\mu}{\ln(L/r) - 1/2}, \quad c_n = \frac{4\pi\mu}{\ln(L/r)+1/2}, \qquad \text{(Equation 1)}$$

taking asymptotic limits for a slender rod, where μ is the dynamic viscosity, and L the length and r the radius of the cirrus. Here, we estimate $2r = 1.5$ μm from Figure 1C.

The total instantaneous drag force on the cirrus is numerically integrated to give

$$F(t) = \sum_{s=0}^{L} f(s, t)\Delta s, \qquad \text{(Equation 2)}$$

and we also define an effective "center of force" to understand the within-beat progression of force:
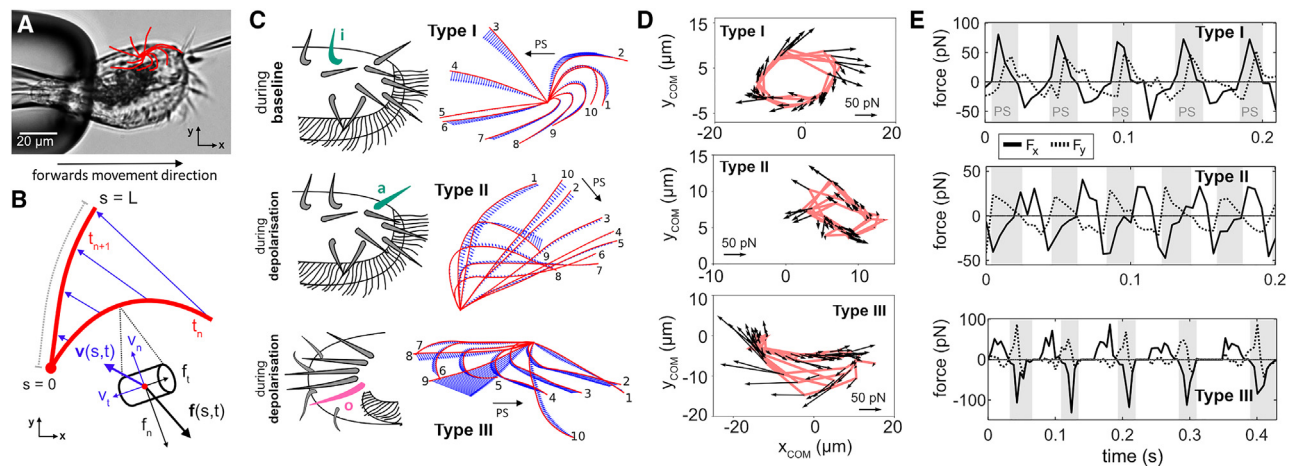
Figure 4. *Euplotes* walking relies on three stereotyped waveforms

(A) Still from a video showing a cell held in ventral view, overlaid with a hand traced waveform of one of the frontoventral cirri (cirrus "i," Figure 1D).

(B) Principle behind RFT estimates for the drag on a slender filament moving through a fluid.

(C) Example tracings (red) over one beat cycle of the three waveform types we observed for a frontoventral cirrus during the baseline state (Type I) or respectively a depolarization event (Type II), and a transverse cirrus during a depolarization event (Type III). (Blue arrows: local force vectors; black arrows: cirri power stroke direction.)

(D) Integrated total $\boldsymbol{F}(t)$ over five beat cycles, localized at the center-of-force coordinates.

(E) x and y components of $\boldsymbol{F}(t)$ (PSs are shaded).

See also Figure S3 and Videos S4, S5, and S6.

$$\boldsymbol{X}(t) = \frac{\sum\limits_{s=0}^{L} |\boldsymbol{f}(s,t)||\boldsymbol{r}(s,t)}{\sum\limits_{s=0}^{L} |\boldsymbol{f}(s,t)|}. \qquad \text{(Equation 3)}$$

From high-speed videos of cells held in different orientations, the 3D nature of cirri beating is apparent. The ventral view, and forces in this x-y plane, are most relevant for walking. We identified three main waveforms: the "normal" circular beat of the frontoventral cirri during the baseline state (Type I), the sideways sweep of the frontoventral cirri during depolarizations (Type II), and the anteriad beating of the transverse cirri, also during depolarizations (Type III) (Figure 4C; Videos S4, S5, and S6). This is a simplification because in reality there is variability across different cirri, and some rarer waveforms appear between modes (Figures 5A and S3; Videos S4, S5, and S6). Nonetheless, classification into these three waveform types broadly captures the key cirri dynamics relevant for understanding whole-cell locomotion. Plotting the force $\boldsymbol{F}(t)$ localized to $\boldsymbol{X}(t)$ over five beat cycles reveals three distinct limit cycles corresponding to the three waveform types (Figure 4D).

To compare propulsive forces produced by the three waveforms (for walking), we project $\boldsymbol{F}(t)$ in the x and y directions. The propulsive force oscillates with the periodic beating of the cirri. In the Type I waveform, associated with baseline membrane potential, cirri power strokes are directed toward the posterior of the cell and correspond to peaks in F_x. The average peak force is $F_x = 75 \pm 5$ pN (n = 5 beat cycles, Figure 4E, Type I). During depolarizations, the beat pattern of the frontoventral cirri is confined to a more anterior orientation with the power stroke toward the right (Type II waveform), with a peak $F_x = -42 \pm 3$ pN and a peak $F_y = 25 \pm 6$ pN during the power strokes (n = 5 cycles, Figure 4E, Type II). Finally, the transverse cirri, which only

become fully active during depolarizations, beat with a power stroke toward the anterior of the cell (Type III waveform) with a peak force $F_x = -111 \pm 17$ pN (n = 5 beat cycles, Figure 4E, Type III).

By tracking cirri waveforms, we identified three representative modes that characterize the main cirri activity patterns during active *Euplotes* walking. We used these shape sequences to estimate the hydrodynamic drag acting on the cirri in each case. The next step is to relate this to the whole-cell dynamics of walking and associated bioelectrical activity.

Membrane potential controls whole-cell walking

To construct a minimal model relating cirri activity to the cell's global walking dynamics, we first observe that the cirri waveforms of freely walking and pipette-held *Euplotes* cells are fundamentally similar and can both be classified by the three waveform types in Figure 4C (Figure S3; Videos S2, S3, S4, S5, S6, and S8). The main difference is that the power stroke of the cirri in freely walking cells is less extended, likely due to surface interactions. This suggests that the cell actuates its cirri in a similar way whether it is swimming or walking. The Type I waveform is used for forward walking, whereas Types II and III only appear during SSR events.

We model whole-cell walking and turning by accounting for the total number of frontoventral or transverse cirri that are active, and their waveforms (Figure 5A). For simplicity, we assume all 15 cirri are located on the ventral surface, along the $y = 0$ centerline of the cell body, with a separation $d = 25\mu m$, either in the anterior or posterior half of the cell (Figure 5B). At any given time, the total drag on all the cirri $\boldsymbol{F}_{cirri} = \boldsymbol{F}_I + \boldsymbol{F}_{II} + \boldsymbol{F}_{III}$, where $\boldsymbol{F}_i$ is the force associated with the Type i waveform, which we take to be $\boldsymbol{F}_i \approx N_{PS,i}\langle\boldsymbol{F}_{PS,i}\rangle + N_{RS,i}\langle\boldsymbol{F}_{RS,i}\rangle$, where $N_{PS,i}$ and $N_{RS,i}$ are the number of active cirri that are found in their power (PS)
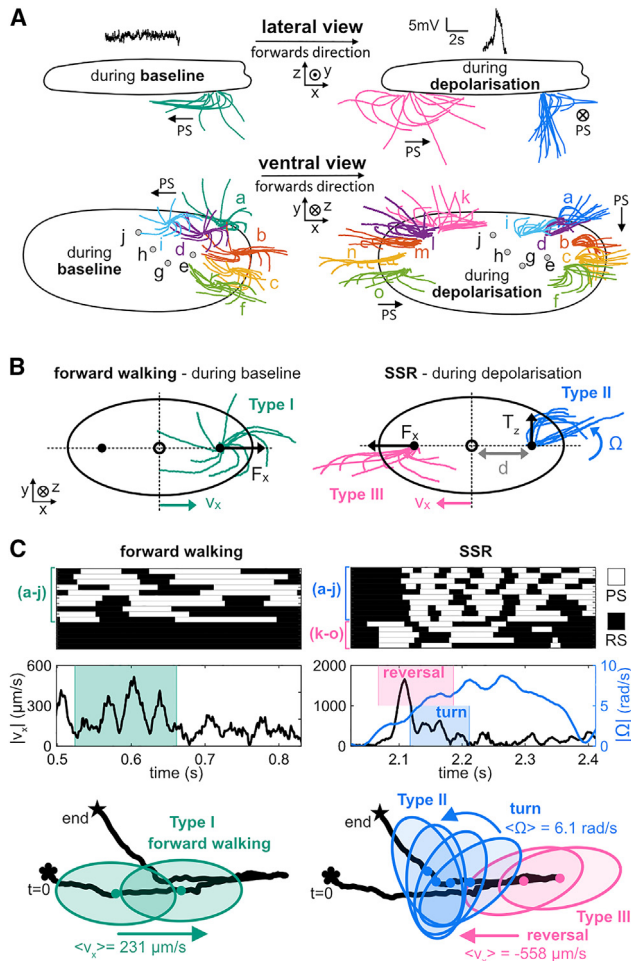
Figure 5. Minimal model for a walking *Euplotes* cell

(A) Overview of the different cirri waveforms observed for different cell orientations and corresponding to the two bioelectric cell states: baseline and depolarization events. (Waveforms traced by hand from experimental footage. PS indicates direction of the cirri power stroke.)

(B) Model of the cell as a prolate spheroid with frontoventral (and transverse) cirri localized to $x = +25$ and $x = -25$ μm, respectively.

(C) From a sample high-speed video of a freely walking cell (Video S2), we annotate the cirri stepping pattern according to whether they are performing a power (PS) or recovery stroke (RS), and in which of the three waveforms (Types I, II, and III). These are shown alongside cell speed v_x and angular velocity Ω at equivalent times. Shaded regions highlight approximately one beat of the cirri in each of the Type I, II, and III waveforms (green, blue, and pink, respectively), which are used to obtain the time-averaged values $\langle v_x \rangle$ and $\langle \Omega \rangle$.

See also Figure S3 and Videos S2, S4, S5, S6, and S8.

or, respectively, recovery stroke (RS) state, and $\langle F_{PS,i} \rangle$ and $\langle F_{RS,i} \rangle$ are the time-averaged RFT forces for the Type i waveform for the power and recovery stroke phases, respectively (see STAR Methods). Similarly, the total torque $T_{cirri} = T_I + T_{II} + T_{III}$, where the torque for the type i waveform is $T_i \approx N_{PS,i} \langle T_{PS,i} \rangle + N_{RS,i} \langle T_{RS,i} \rangle$. For the Type I and II waveforms, $N_{RS} = 10 - N_{PS}$, while for the Type III waveform, $N_{RS} = 5 - N_{PS}$. For each waveform type, we use the previous RFT estimates from pipette-held cells to approximate the drag for the cirri of freely walking cells.

For low-Reynolds number propulsion, the thrust generated by the cirri is balanced by the drag on the cell body, similarly for the torque. This is accurate for cells swimming through bulk fluid but is only an approximation for cells moving across surfaces, where cells may experience other forces, such as adhesion through direct interaction of the cirri with the substrate. Here, we neglect adhesion, and focus only on the hydrodynamic drag (see discussion).

The cell body is estimated as a prolate spheroid,[81,82] with semi-major and minor axis dimensions to be $a = 42 \pm 3$μm (n = 14 cells), $b = 20 \pm 2$ μm (n = 8 cells), and eccentricity $e = \sqrt{1 - (b^2/a^2)} \approx 0.88$. The viscous drag and torque are given by

$$F_x^* = 6\pi\mu a v_x C_1, \quad \text{(Equation 4A)}$$

$$F_y^* = 6\pi\mu a v_y C_2, \quad \text{(Equation 4B)}$$

$$T_z^* = 8\pi\mu a b^2 \Omega C_3, \quad \text{(Equation 4C)}$$

where v_x and v_y are the x and y components of the cell velocity, Ω is the angular velocity, μ is the fluid viscosity, and

$$C_1 = \frac{8}{3}e^3 \left[-2e + (1+e^2)\ln\frac{1+e}{1-e} \right]^{-1}, \quad \text{(Equation 5A)}$$

$$C_2 = \frac{16}{3}e^3 \left[2e + (3e^2 - 1)\ln\frac{1+e}{1-e} \right]^{-1}, \quad \text{(Equation 5B)}$$

$$C_3 = \frac{4}{3}e^3 \frac{2-e^2}{1-e^2} \left[-2e + (1+e^2)\ln\frac{1+e}{1-e} \right]^{-1}. \quad \text{(Equation 5C)}$$

The equations for a sphere are recovered when $e \to 0$.

Next, we validate the model against data by comparing the number of active cirri contributing to either forward walking or an SSR. From a short recording (265 frames, 800 fps) of a forward walking cell, we manually annotated the activity of each frontoventral cirrus (a–j).[33,34] We define an active cirrus as being either in the PS or RS phase of the Type I waveform (Figure 5C) and estimated the speed v_x in the x direction. Over one beat cycle, $\langle v_x \rangle = 231$ μm s^{-1}. Substituting this into Equation 4, we find $F_x^* = 106$ pN. Because walking is primarily due to the frontoventral cirri in the Type I waveform, the force balance in the x direction is given by $F_x^* = N_{PS,I}\langle F_{x,PS,I} \rangle + (10 - N_{PS,I})\langle F_{x,RS,I} \rangle$. For the Type I waveform, we estimated $\langle F_{x,PS} \rangle = 33 \pm 5$ pN and $\langle F_{x,RS} \rangle = -19 \pm 2$ pN for the PS and RS phases, respectively. This gives us $N_{PS,I} = 5.7$, which agrees well with $\langle N_{PS,I} \rangle \approx 5.9$ obtained from direct tracking of cirri activity (see STAR Methods). This means *Euplotes* forward walking is driven by ~6 of its 10 frontoventral cirri simultaneously being in the power stroke phase.

From a recording of a sample SSR (310 frames, 800 fps), we again annotated cirri activity according to whether the cirri are in the PS or RS phase of the Type II or Type III waveform (Figure 5C). The SSR, which corresponds to depolarizations, consists of two phases: a fast backward motion followed by a turn about the cell's axis (yaw). Recall that SSRs are highly stereotyped, with average duration 0.30 ± 0.09 s, and a reproducible counterclockwise turning angle $|\alpha| = 113 \pm 18°$, viewed from the ventral side. The propulsion speed in the x direction of the cell v_x and angular velocity Ω is again calculated. Over a period

Table 1. A comparison between experimental measurements and a mechanical model of whole-cell walking in *Euplotes*

Gait:	Forward walking	SSR (turn)	SSR (reversal)
Bioelectric state:	baseline	depolarization	depolarization
Waveform:	Type I	Type II	Type III
Power stroke:	$\langle F_{x,PS} \rangle = 33 \pm 5$ pN	$\langle T_{z,PS} \rangle = 542 \pm 37$ pN μm	$\langle F_{x,PS} \rangle = -51 \pm 4$ pN
Recovery stroke:	$\langle F_{x,RS} \rangle = -19 \pm 2$ pN	$\langle T_{z,RS} \rangle = -394 \pm 66$ pN μm	$\langle F_{x,RS} \rangle = 13 \pm 2$ pN
Speed (from trajectory):	$\langle v_x \rangle = 231$ μm s^{-1}	$\langle \Omega \rangle = 6.1$ rad/s	$\langle v_x \rangle = -558$ μm s^{-1}
N_{PS}(model):	5.7	8.6	5.0
N_{PS}(counting):	5.9	7.1	3.4

Summary statistics from RFT estimates for the time-averaged forces and torques during the power and recovery stroke for each of the three different waveform types (data from n = 5 PS and 4 RS strokes, respectively). Average speed v_x, and angular velocity Ω values were estimated from a high-speed video of a freely moving cell (Video S2). N_{PS}(model) and N_{PS}(counting) are estimates for the number of cirri in the power stroke phase of the relevant waveform contributing to each of the three distinct phases of activity considered in the text, obtained either from our minimal model, or by direct counting.

of one beat cycle during the backward motion of the transverse cirri, $\langle v_x \rangle = -558$ μm s^{-1}. From Equation 4, we obtain $F_x^* = -258$ pN. The backward motion is largely generated by the Type III waveform of the transverse cirri (k–o), which leads to the force balance $F_x^* = N_{PS,III}\langle F_{x,PS} \rangle + (5 - N_{PS,III})\langle F_{x,RS} \rangle$. For the Type III waveform, we estimated $\langle F_{x,PS} \rangle = -51 \pm 4$ pN and $\langle F_{x,RS} \rangle = 13 \pm 2$ pN for the PS and RS phases, respectively. This gives $N_{PS,III} = 5.0$, compared with $\langle N_{PS,III} \rangle \approx 3.4$ obtained from direct annotation.

Finally, for the turning phase of the SSR, over one beat period, we estimated $\langle \Omega \rangle = 6.1$ rad/s. From Equation 4, we obtain $T_z^* = 4.1 \times 10^3$ pN μm. If cell turning is driven exclusively by the frontoventral cirri performing the Type II beat pattern, then the torque balance gives $T_z^* = N_{PS,II}\langle T_{z,PS} \rangle + (10 - N_{PS,II})\langle T_{z,RS} \rangle$. Using RFT to estimate torques $\mathbf{T}(t) = \sum_{s=0}^{L} \mathbf{r}(s) \times \mathbf{f}(s,t)\Delta s$, where $\mathbf{r}(s)$ is the position relative to the center of the cell, we estimate for the Type II waveform $\langle T_{z,PS} \rangle = 542 \pm 37$ pN μm and $\langle T_{z,RS} \rangle = -394 \pm 66$ pN μm for the PS and RS phases, respectively. This gives $N_{PS,II} = 8.6$, compared with $\langle N_{PS,II} \rangle \approx 7.1$ obtained from counting cirri activity.

Our simplified picture (Table 1) provides estimates for the number of cirri that are active in each gait. The agreement with data is best for forward walking, but the model overestimates the number of transverse cirri during reversals. This is likely because it neglects the frontoventral cirri, which during this phase also contributes to backward movement. Meanwhile, SSRs require more synchronized or concerted action of the cirri. We have shown that the cell's membrane potential can be classified into two bioelectric states (baseline and depolarizations). These are linked to two distinct modes of the cirri, which, in turn, maps to two distinct locomotor gaits (forward walking and SSRs), during which the frontoventral and transverse cirri display three possible beating patterns.

DISCUSSION

Ciliates embody many behaviors that are reminiscent of locomoting animals, in which modular movements are chained together to generate complex stimulus-response sequences.[25] Time and again, these remarkable feats call into question what is physiologically possible within a single cell, reviving its depiction as a "swimming neuron."[14,83] Here, we have identified a

low-dimensional-state space for *Euplotes'* walking dynamics and mapped its discrete behaviors to discrete bioelectric states by simultaneous high-speed imaging and electrophysiology. We demonstrated the heterogeneity of different cirri on the same cell, with different groups of cirri behaving differently. We also presented a mechanistic picture of how membrane potential precisely orchestrates cirri movement, leading to dynamic and reversible switching between whole-cell walking or turning.

A substantial literature already implicates bioelectric signaling in controlling the motility of diverse protists.[48,84–86] *Paramecium*, an extensively studied system, exhibits a characteristic avoidance response involving a backward motion followed by a turn before resumption of forward swimming.[16,50] Although reversals are triggered by action potentials, visualizing cilia activity at the same time as membrane potential has proven difficult. A recent study used changes in flow patterns around the cell as a proxy for depolarization-induced changes in cilia-beat direction.[55] Previous research on the walking ciliates, although somewhat inconclusive, suggested a much more nuanced response of the cirri to potential modulation, in contrast to the *en masse* ciliary reversals observed in *Paramecium*. In *Euplotes*, short depolarizations above a threshold can slow down the cirri, while extended periods of depolarization can reverse the cirri beat orientation.[62,63] Yet, other studies show that on depolarization cirri orientation immediately reverses, while on hyperpolarization, cirri beat frequency increases.[65–67] In *Stylonychia*, cirri motor responses can be elicited by positive or negative shifts from its resting potential,[68,69] with depolarizations associated with Ca^{2+} influx and an anteriorly oriented power stroke qualitatively similar to our Type II waveform, while hyperpolarizations are associated with a Ca^{2+} efflux and a posteriorly oriented power stroke similar to our Type I waveform.[69,87,88]

Here, by imaging *Euplotes* cirri movement simultaneously with electrophysiology recordings, we unequivocally demonstrated the coupling between membrane potential, cirri beating, and whole-cell walking motility. Our detailed and integrative analyses resolved changes in cirri beating and detected an $\mathcal{O}(100)$ ms latency in the response of cirral parameters to changes in membrane potential. Therefore, cirri likely do not respond directly to membrane potential but rather to voltage-gated calcium channels, which regulate intraciliary Ca^{2+} and alter the conformation of dyneins.[53,89] This gating timescale is

comparable to that estimated for *Chlamydomonas* phototaxis and the *Paramecium* avoiding reaction.[50,78]

The timing (duration, frequency) of the SSR turning events may be under cellular bioelectric control. Mixed-mode motility strategies combining steady forward movement with fast reorientations are common in microbes.[20,90] Modulating the balance of different motility modes in response to chemical cues could enable *Euplotes* to perform chemokinesis and increase the dwell time in nutrient-rich areas.[63] Moreover, depending on the ecological context, different species may employ distinct motility strategies with stereotyped turning angles (here, ~110°) to enhance the efficacy of environmental sampling.[91–93] While *Euplotes* SSR events are rapid ($\mathcal{O}(100)$ ms), they are much slower than neuronal signaling; indeed, *Euplotes* membrane depolarizations are not *bona fide* action potentials.

We remark on some differences observed between pipette-held and freely walking cells. Cells immobilized on micropipettes exhibited longer spontaneous membrane depolarizations than freely walking cells (as inferred from duration of SSRs), and the "stop" state was rarely observed. Cirri beat frequency was also more variable, even though the associated patterns of cirri beating are similar (Figure S3). A previous study in *Euplotes* suggested a regular rhythm of spontaneous depolarizations,[62] but our more comprehensive dataset showed a high degree of cell-to-cell variability. Our use of a second holding pipette to immobilize the cell for high-resolution imaging may have contributed to deviations from true spontaneous activity that would otherwise be experienced by a cell that is completely free to move. Such differences hint at a mechanosensitive ("touch") response of *Euplotes*,[66,67] which remains to be further explored, especially in combination with other chemical or ionic perturbations.

Our mechanical model, which couples cirri activity to whole-cell locomotion, is well supported by the data. However, we focused only on surface-based walking and did not account for adhesion. Based on measurements of *Chlamydomonas* gliding motility, if an entire 12.5 μm-flagellum (fully attached to the substrate) produces approximately 0.5 nN of force,[94] then a cirrus that only temporarily contacts the surface at the tip ($\leq$ 0.5 μm) can be expected to produce $\leq$20 pN of force during peak contact, lower than hydrodynamic drag.

A hallmark of biological cognition is the capacity to rapidly control complex actions from a distance. In *Euplotes*, we found striking functional differences between distinct groups of cirri (Figure 1). Other protists also have heterogeneous ciliary structures with distinct functions: the flagellar apparatuses of algae,[19] the ciliary bands of *Didinium*,[54] and the membranelle bands of *Stentor*.[70] Even cilia that appear morphologically similar may have divergent functions. *Chlamydomonas* phototaxis requires opposing responses of the two cilia[95,96] to Ca²⁺,[97] while the four isokont cilia of some quadriflagellates can start and stop beating at different times.[33] Here, distinct groups of cirri in a *Euplotes* cell responded differently to the *same bioelectric signal* during SSRs. We suggest two mechanisms for this functional asymmetry. First, there may be a heterogeneous distribution of voltage-sensitive ion channels around the cell, hypothesized to explain the differential response in *Paramecium* to mechanical stimulation at the posterior vs anterior.[98] Alternatively, inherent asymmetries in the cytoskeletal or cortical architecture may contribute to active control of ciliary activity and whole-body coordination.[32,34]

Our work on the walking ciliate *Euplotes* reveals new complexity in the bioelectrical regulation of ciliary activity and how this control architecture can vary even across different unicellular species. Ultimately these insights can help us understand how divergent motor responses can arise on the same cell, and the origins of bioelectrical communication in living systems.

STAR★METHODS

Detailed methods are provided in the online version of this paper and include the following:

- ● KEY RESOURCES TABLE
- ● RESOURCE AVAILABILITY
  - ○ Lead contact
  - ○ Materials availability
  - ○ Data and code availability
- ● EXPERIMENTAL MODEL AND SUBJECT DETAILS
  - ○ Cell culturing
  - ○ Species classification
- ● METHOD DETAILS
  - ○ Scanning electron microscopy
  - ○ DAPI staining and confocal imaging
  - ○ Experimental solutions
  - ○ Imaging and tracking the behaviour of freely moving cells
  - ○ Trajectory analysis
  - ○ Assignment of motility states
  - ○ SSR characteristics
  - ○ Distribution fits
  - ○ Electrophysiology and high-speed imaging
  - ○ Analysis of membrane depolarisation events
  - ○ Cirri frequency analysis
  - ○ Cross-correlations
  - ○ Tracking cirri using SLEAP
  - ○ Probability flux of SLEAP-tracked cirri tips
  - ○ Cirri beat characteristics for SLEAP-tracked cirri
  - ○ RFT and model calculations
  - ○ Manual annotation of cirri activity
- ● QUANTIFICATION AND STATISTICAL ANALYSIS

AUTHOR CONTRIBUTIONS

Conceptualization, H.L.-S. and K.Y.W.; methodology, H.L.-S. and K.Y.W.; investigation, H.L.-S. and K.Y.W.; software, H.L.-S.; formal analysis, H.L.-S.;

Current Biology
Article

REFERENCES

1. Miller, C.T., Gire, D., Hoke, K., Huk, A.C., Kelley, D., Leopold, D.A., Smear, M.C., Theunissen, F., Yartsev, M., and Niell, C.M. (2022). Natural behavior is the language of the brain. Curr. Biol. *32*, R482–R493.

2. Stephens, G.J., Bueno de Mesquita, M., Ryu, W.S., and Bialek, W. (2011). Emergence of long timescales and stereotyped behaviors in Caenorhabditis elegans. Proc. Natl. Acad. Sci. USA *108*, 7286–7289.

3. Yemini, E., Jucikas, T., Grundy, L.J., Brown, A.E., and Schafer, W.R. (2013). A database of Caenorhabditis elegans behavioral phenotypes. Nat. Methods *10*, 877–879.

4. Wan, K.Y., and Jékely, G. (2021). Origins of eukaryotic excitability. Philos. Trans. R. Soc. Lond. B Biol. Sci. *376*, 20190758.

5. Roberts, R.J.V., Pop, S., and Prieto-Godino, L.L. (2022). Evolution of central neural circuits: state of the art and perspectives. Nat. Rev. Neurosci. *23*, 725–743.

6. Lyon, P., Keijzer, F., Arendt, D., and Levin, M. (2021). Reframing cognition: getting down to biological basics. Philos. Trans. R. Soc. Lond. B Biol. Sci. *376*, 20190750.

7. Verni, F., and Gualtieri, P. (1997). Feeding behaviour in ciliated protists. Micron *28*, 487–504.

8. Nilsson, D.E., and Marshall, J. (2020). Lens eyes in protists. Curr. Biol. *30*, R458–R459.

9. Leander, B.S. (2020). Predatory protists. Curr. Biol. *30*, R510–R516.

10. Ricci, N. (1990). The behaviour of ciliated protozoa. Anim. Behav. *40*, 1048–1069.

11. Rajan, D., Makushok, T., Kalish, A., Acuna, L., Bonville, A., Correa Almanza, K., Garibay, B., Tang, E., Voss, M., Lin, A., et al. (2023). Single-cell analysis of habituation in Stentor coeruleus. Curr. Biol. *33*, 241–251.e4.

12. Dexter, J.P., Prabakaran, S., and Gunawardena, J. (2019). A Complex Hierarchy of Avoidance Behaviors in a Single-Cell Eukaryote. Curr. Biol. *29*, 4323–4329.e2.

13. Gershman, S.J., Balbi, P.E., Gallistel, C.R., and Gunawardena, J. (2021). Reconsidering the evidence for learning in single cells. eLife *10*, e61907.

14. Brette, R. (2021). Integrative Neuroscience of *Paramecium*, a "Swimming Neuron". eNeuro. eNeuro *8*, 18–21.2021.

15. Hamel, A., Fisch, C., Combettes, L., Dupuis-Williams, P., and Baroud, C.N. (2011). Transitions between three swimming gaits in *Paramecium* escape. Proc. Natl. Acad. Sci. USA *108*, 7290–7295.

16. Jennings, H.S. (1906). Behavior of the Lower Organisms (Columbia University Press).

17. Berg, H.C., and Purcell, E.M. (1977). Physics of chemoreception. Biophys. J. *20*, 193–219.

18. Wadhwa, N., and Berg, H.C. (2022). Bacterial motility: machinery and mechanisms. Nat. Rev. Microbiol. *20*, 161–173.

19. Wan, K.Y., and Goldstein, R.E. (2018). Time Irreversibility and Criticality in the Motility of a Flagellate Microorganism. Phys. Rev. Lett. *121*, 58103.

20. Bentley, S.A., Laeverenz-Schlogelhofer, H., Anagnostidis, V., Cammann, J., Mazza, M.G., Gielen, F., and Wan, K.Y. (2022). Phenotyping single-cell motility in microfluidic confinement. eLife *11*, e76519.

21. Polin, M., Tuval, I., Drescher, K., Gollub, J.P., and Goldstein, R.E. (2009). *Chlamydomonas* Swims with Two "Gears" in a Eukaryotic Version of Run-and-Tumble Locomotion. Science *325*, 487–490.

22. Echigoya, S., Sato, K., Kishida, O., Nakagaki, T., and Nishigami, Y. (2022). Switching of behavioral modes and their modulation by a geometrical cue in the ciliate stentor coeruleus. Front. Cell Dev. Biol. *10*, 1021469.

23. Coyle, S.M., Flaum, E.M., Li, H., Krishnamurthy, D., and Prakash, M. (2019). Coupled Active Systems Encode an Emergent Hunting Behavior in the Unicellular Predator Lacrymaria olor. Curr. Biol. *29*, 3838–3850.e3.

24. Wan, K.Y. (2019). Ciliate Biology: The Graceful Hunt of a Shape-Shifting Predator. Curr. Biol. *29*, R1174–R1176.

25. Marques, J.C., Lackner, S., Félix, R., and Orger, M.B. (2018). Structure of the Zebrafish Locomotor Repertoire Revealed with Unsupervised Behavioral Clustering. Curr. Biol. *28*, 181–195.e5.

26. Mearns, D.S., Donovan, J.C., Fernandes, A.M., Semmelhack, J.L., and Baier, H. (2020). Deconstructing Hunting Behavior Reveals a Tightly Coupled Stimulus-Response Loop. Curr. Biol. *30*, 54–69.e9.

27. Gomez-Marin, A., Stephens, G.J., and Louis, M. (2011). Active sampling and decision making in Drosophila chemotaxis. Nat. Commun. *2*, 441.

28. Marder, E., and Bucher, D. (2001). Central pattern generators and the control of rhythmic movements. Curr. Biol. *11*, R986–R996.

29. Yamamoto, W., and Yuste, R. (2023). Peptide-driven control of somersaulting in Hydra vulgaris. Curr. Biol. *33*, 1893–1905.e4.

30. Marshall, W.F. (2011). Origins of cellular geometry. BMC Biol. *9*, 57.

31. Aufderheide, K.J., Frankel, J., and Williams, N.E. (1980). Formation and positioning of surface-related structures in protozoa. Microbiol. Rev. *44*, 252–302.

32. Wan, K.Y., and Goldstein, R.E. (2016). Coordinated beating of algal flagella is mediated by basal coupling. Proc. Natl. Acad. Sci. USA *113*, E2784–E2793.

33. Wan, K.Y. (2020). Synchrony and symmetry-breaking in active flagellar coordination. Philos. Trans. R. Soc. Lond. B Biol. Sci. *375*, 20190393.

34. Larson, B.T., Garbus, J., Pollack, J.B., and Marshall, W.F. (2022). A unicellular walker controlled by a microtubule-based finite-state machine. Curr. Biol. *32*, 3745–3757.e7.

35. Soh, A.W.J., Woodhams, L.G., Junker, A.D., Enloe, C.M., Noren, B.E., Harned, A., Westlake, C.J., Narayan, K., Oakey, J.S., Bayly, P.V., et al. (2022). Intracellular connections between basal bodies promote the coordinated behavior of motile cilia. Mol. Biol. Cell *33*, br18.

36. Salisbury, J.L. (1988). The lost neuromotor apparatus of *chlamydomonas*: rediscovered. J. Protozool. *35*, 574–577.

37. Roth, L.E. (1957). An electron microscope study of the cytology of the protozoan Euplotes patella. J. Biophys. Biochem. Cytol. *3*, 985–1000.

38. Hodgkin, A.L., and Huxley, A.F. (1952). A quantitative description of membrane current and its application to conduction and excitation in nerve. J. Physiol. *117*, 500–544.

39. Levin, M. (2021). Bioelectric signaling: Reprogrammable circuits underlying embryogenesis, regeneration, and cancer. Cell *184*, 1971–1989.

40. Schofield, Z., Meloni, G.N., Tran, P., Zerfass, C., Sena, G., Hayashi, Y., Grant, M., Contera, S.A., Minteer, S.D., Kim, M., et al. (2020). Bioelectrical understanding and engineering of cell biology. J. R. Soc. Interface *17*, 20200013.

41. Salvador-Recatalà, V., Tjallingii, W.F., and Farmer, E.E. (2014). Real-time, *in vivo* intracellular recordings of caterpillar-induced depolarization waves in sieve elements using aphid electrodes. New Phytol. *203*, 674–684.

42. Simons, P.J. (1981). The role of electricity in plant movements. New Phytol. *87*, 11–37.

43. Cohen, D.J., Nelson, W.J., and Maharbiz, M.M. (2014). Galvanotactic control of collective cell migration in epithelial monolayers. Nat. Mater. *13*, 409–417.

44. Zhao, M., Rolandi, M., and Isseroff, R.R. (2022). Bioelectric Signaling: Role of Bioelectricity in Directional Cell Migration in Wound Healing. Cold Spring Harb. Perspect. Biol. *14*. Place.

45. Kikuchi, K., Galera-Laporta, L., Weatherwax, C., Lam, J.Y., Moon, E.C., Theodorakis, E.A., Garcia-Ojalvo, J., and Süel, G.M. (2022). Electrochemical potential enables dormant spores to integrate environmental signals. Science *378*, 43–49.

46. Prindle, A., Liu, J., Asally, M., Ly, S., Garcia-Ojalvo, J., and Süel, G.M. (2015). Ion channels enable electrical communication in bacterial communities. Nature *527*, 59–63.

47. Liu, J., Prindle, A., Humphries, J., Gabalda-Sagarra, M., Asally, M., Lee, D.Y., Ly, S., Garcia-Ojalvo, J., and Süel, G.M. (2015). Metabolic co-dependence gives rise to collective oscillations within biofilms. Nature *523*, 550–554.

48. Eckert, R., and Naito, Y. (1972). Bioelectric control of locomotion in the ciliates. J. Protozool. *19*, 237–243.

49. Naitoh, Y. (1974). Bioelectric Basis of Behavior in Protozoa. Am. Zool. *14*, 883–893.

50. Machemer, H., and Eckert, R. (1973). Electrophysiological Control of Reversed Ciliary Beating in *Paramecium*. J. Gen. Physiol. *61*, 572–587.

51. de Peyer, J.E., and Machemer, H. (1978). Hyperpolarizing and Depolarizing Mechanoreeeptor Potentials in Stylonychia. J. Comp. Physiol. *127*, 255–266.

52. De Peyer, J.E., and Machemer, H. (1982). Electromechanical coupling in cilia I. Effects of depolarizing voltage steps. Cell Motil. *2*, 483–496.

53. Krüppel, T., and Wissing, F. (1996). Characterisation of the voltagemactivated calcium current in the marine ciliate Euplotes vannus. Cell Calcium *19*, 229–241.

54. Pape, H.-C., and Machemer, H. (1986). Electrical properties and membrane currents in the ciliateDidinium. J. Comp. Physiol. *158*, 111–124.

55. Elices, I., Kulkarni, A., Escoubet, N., Pontani, L.L., Prevost, A.M., and Brette, R. (2023). An electrophysiological and kinematic model of Paramecium, the "swimming neuron". PLOS Comput. Biol. *19*, e1010899.

56. Machemer, H. (1989). Cellular Behaviour Modulated by Ions: Electrophysiological Implications. J. Protozool. *36*, 463–487.

57. Deitmer, J.W., Machemer, H., and Martinac, B. (1984). Motor control in three types of ciliary organelles in the ciliate stylonychia. J. Comp. Physiol. *154*, 113–120.

58. Boscaro, V., Syberg-Olsen, M.J., Irwin, N.A.T., Del Campo, J., and Keeling, P.J. (2019). What Can Environmental Sequences Tell Us About the Distribution of Low-Rank Taxa? The Case of *Euplotes* (Ciliophora, Spirotrichea), Including a Description of *Euplotes enigma* sp. nov. J. Eukaryot. Microbiol. *66*, 281–293.

59. Ricci, N., Giannetti, R., and Miceli, C. (1988). The ethogram of euplotes crassus (ciliata, hypotrichida): I. the wild type. Eur. J. Protistol. *23*, 129–140.

60. Schmidt, J.A., and Eckert, R. (1976). Calcium couples flagellar reversal to photostimulation in Chlamydomonas reinhardtii. Nature *262*, 713–715.

61. Fujiu, K., Nakayama, Y., Yanagisawa, A., Sokabe, M., and Yoshimura, K. (2009). Chlamydomonas cav2 encodes a voltage-dependent calcium channel required for the flagellar waveform conversion. Curr. Biol. *19*, 133–139.

62. Lueken, W., Ricci, N., and Krüppel, T. (1996). Rhythmic spontaneous depolarizations determine a slow-and-fast rhythm in walking of the marine hypotrich euplotes vannus. Eur. J. Protistol. *32*, 47–54.

63. Stock, C., Krüppel, T., and Lueken, W. (1997). Kinesis in euplotes vannus-ethological and electrophysiological characteristics of chemosensory behavior. J. Eukaryot. Microbiol. *44*, 427–433.

64. Stock, C., Krüppel, T., Key, G., and Lueken, W. (1999). Sexual behaviour in Euplotes raikovi is accompanied by pheromone-induced modifications of ionic currents. J. Exp. Biol. *202*, 475–483.

65. Epstein, M., and Eckert, R. (1973). Membrane Control of Ciliary Activity in the Protozoan Euplotes. J. Exp. Biol. *58*, 437–462.

66. Krüppel, T., Rabe, H., Dümmler, B., and Lueken, W. (1995). The depolarizing mechanoreceptor potential and ca/mg receptor-current of the marine ciliate euplotes vannus. J. Comp. Physiol. A *177*, 511–517.

67. Krüppel, T., Furchbrich, V., and Leuken, W. (1993). Electrical responses of the marine ciliate euplotes vannus (Hypotrichia) to mechanical stimulation at the posterior cell end. J. Membr. Biol. *135*, 253–260.

68. Mogami, Y., Pernberg, J., and Machemer, H. (1992). Ciliary beating in three dimensions: steps of a quantitative description. J. Math. Biol. *30*, 215–249.

69. Mogami, Y., and Machemer, H. (1991). In vivo activation of cirral movement in stylonychia by calcium. J. Comp. Physiol. A *168*, 687–695.

70. Wan, K.Y., Hürlimann, S.K., Fenix, A.M., McGillivary, R.M., Makushok, T., Burns, E., Sheung, J.Y., and Marshall, W.F. (2020). Reorganization of complex ciliary flows around regenerating *Stentor coeruleus*. Philos. Trans. R. Soc. Lond. B Biol. Sci. *375*, 20190167.

71. Rode, M., Kiørboe, T., and Andersen, A. (2022). Feeding flow and membranele filtration in ciliates. Phys. Rev. Fluids *7*, 23102.

72. Erra, F., Iervasi, A., Ricci, N., and Banchetti, R. (2001). Movement of the cirri during the creeping of euplotes crassus (ciliata, hypotrichida). Can. J. Zool. Can. De Zool. *79*, 1353–1362.

73. Pereira, T.D., Tabris, N., Matsliah, A., Turner, D.M., Li, J., Ravindranath, S., Papadoyannis, E.S., Normand, E., Deutsch, D.S., Wang, Z.Y., et al. (2022). Sleap: A deep learning system for multi-animal pose tracking. Nat. Methods *19*, 486–495.

74. Cammann, J., Schwarzendahl, F.J., Ostapenko, T., Lavrentovich, D., Bäumchen, O., and Mazza, M.G. (2020). Boundary-interior principle for microbial navigation in geometric confinement. arXiv.

75. Battle, C., Broedersz Chase, P., Nikta, F., Geyer Veikko, F., Jonathon, H., Schmidt Christoph, F., and MacKintosh Fred, C. (2016). Broken detailed balance at mesoscopic scales in active biological systems. Science *352*, 604–607.

76. Lighthill, J. (1976). Flagellar Hydrodynamics. SIAM Rev. *18*, 161–230.

77. Gaffney, E.A., Gadêlha, H., Smith, D.J., Blake, J.R., and Kirkman-Brown, J.C. (2011). Mammalian Sperm Motility: Observation and Theory. Annu. Rev. Fluid Mech. *43*, 501–528.

78. Leptos, K.C., Chioccioli, M., Furlan, S., Pesci, A.I., and Goldstein, R.E. (2023). Phototaxis of chlamydomonas arises from a tuned adaptive photoresponse shared with multicellular volvocine green algae. Phys. Rev. E *107*, 14404.

79. Brumley, D.R., Wan, K.Y., Polin, M., and Goldstein, R.E. (2014). Flagellar synchronization through direct hydrodynamic interactions. eLife *3*, e02750.

80. Friedrich, B.M., Riedel-Kruse, I.H., Howard, J., and Jülicher, F. (2010). High-precision tracking of sperm swimming fine structure provides strong test of resistive force theory. J. Exp. Biol. *213*, 1226–1234.

81. Chwang, A.T., and Wu, T.Y. (1975). Hydromechanics of low-Reynolds-number flow. Part 2. Singularity method for Stokes flows. J. Fluid Mech. *67*, 787–815.

82. Bayly, P.V., Lewis, B.L., Ranz, E.C., Okamoto, R.J., Pless, R.B., and Dutcher, S.K. (2011). Propulsive forces on the flagellum during locomotion of Chlamydomonas reinhardtii. Biophys. J. *100*, 2716–2725.

83. Kung, C., and Saimi, Y. (1985). Chapter 3: Ca2+ channels of paramecium: a multidisciplinary study. Current Topics in Membranes and Transport *23*, 45–66. Elsevier.

84. Hegemann, P. (1997). Vision in microalgae. Planta *203*, 265–274.

85. Helliwell, K.E., Chrachri, A., Koester, J.A., Wharam, S., Verret, F., Taylor, A.R., Wheeler, G.L., and Brownlee, C. (2019). Alternative Mechanisms for Fast Na+/Ca2+ Signaling in Eukaryotes via a Novel Class of Single-Domain Voltage-Gated Channels. Curr. Biol. *29*, 1503–1511.e6.

86. Echevarria, M.L., Wolfe, G.V., and Taylor, A.R. (2016). Feast or flee: Bioelectrical regulation of feeding and predator evasion behaviors in

the planktonic alveolate favella sp. (spirotrichia). J. Exp. Biol. *219*, 445–456.

87. Sugino, K., and Machemer, H. (1988). The ciliary cycle during hyperpolarization-induced activity: An analysis of axonemal functional parameters. Cell Motil. Cytoskeleton *11*, 275–290.

88. Mogami, Y., Pernberg, J., and Machemer, H. (1990). Messenger role of calcium in ciliary electromotor coupling: a reassessment. Cell Calcium *11*, 665–673.

89. Sakato, M., Sakakibara, H., and King, S.M. (2007). *Chlamydomonas* Outer Arm Dynein Alters Conformation in Response to Ca²⁺. Mol. Biol. Cell *18*, 3620–3634.

90. Otte, S., Ipiña, E.P., Pontier-Bres, R., Czerucka, D., and Peruani, F. (2021). Statistics of pathogenic bacteria in the search of host cells. Nat. Commun. *12*, 1990.

91. Ricci, N. (1989). Microhabitats of ciliates: Specific adaptations to different substrates. Limnol. Oceanogr. *34*, 1089–1097.

92. Fenchel, T., and Blackburn, N. (1999). Motile Chemosensory Behaviour of Phagotrophic Protists: Mechanisms for and Efficiency in Congregating at Food Patches. Protist *150*, 325–336.

93. Hartl, B., Hübl, M., Kahl, G., and Zöttl, A. (2021). Microswimmers learning chemotaxis with genetic algorithms. Proc. Natl. Acad. Sci. USA *118*, e2019683118.

94. Kreis, C.T., Le Blay, M., Linne, C., Makowski, M.M., and Bäumchen, O. (2018). Adhesion of Chlamydomonas microalgae to surfaces is switchable by light. Nature Phys. *14*, 45–49.

95. Dutcher, S.K. (2020). Asymmetries in the cilia of *Chlamydomonas*. Philos. Trans. R. Soc. Lond. B Biol. Sci. *375*, 20190153.

96. Wan, K.Y., Leptos, K.C., and Goldstein, R.E. (2014). Lag, lock, sync, slip: the many 'phases' of coupled flagella. J. R. Soc. Interface *11*, 20131160.

97. Kamiya, R., and Witman, G.B. (1984). Submicromolar levels of calcium control the balance of beating between the two flagella in demembranated models of Chlamydomonas. J. Cell Biol. *98*, 97–107.

98. Ogura, A., and Machemer, H. (1980). Distribution of mechanoreceptor channels in theParamecium surface membrane. J. Comp. Physiol. *135*, 233–242.

99. Schindelin, J., Arganda-Carreras, I., Frise, E., Kaynig, V., Longair, M., Pietzsch, T., Preibisch, S., Rueden, C., Saalfeld, S., Schmid, B., et al. (2012). Fiji: an open-source platform for biological-image analysis. Nat. Methods *9*, 676–682.

100. Tinevez, J.Y., Perry, N., Schindelin, J., Hoopes, G.M., Reynolds, G.D., Laplantine, E., Bednarek, S.Y., Shorte, S.L., and Eliceiri, K.W. (2017). TrackMate: An open and extensible platform for single-particle tracking. Methods *115*, 80–90.

101. Edelstein, A., Amodaj, N., Hoover, K., Vale, R., and Stuurman, N. (2010). Computer control of microscopes using μmanager. Curr. Protoc. Mol. Biol. *92*, 14.20.1–14.20.17.

102. Callahan, B.J., McMurdie, P.J., Rosen, M.J., Han, A.W., Johnson, A.J.A., and Holmes, S.P. (2016). Dada2: High-resolution sample inference from Illumina amplicon data. Nat. Methods *13*, 581–583.

103. Illumina (2013). 16s Metagenomic Sequencing Library Preparation.

104. Curds, C.R. (1975). A guide to the species of the genus euplotes (hypotrichida, ciliata). Bull. Brit. Mus. Nat. Hist. (Zool.) *28*, 1–68.

105. Syberg-Olsen, M.J., Irwin, N.A., Vannini, C., Erra, F., Di Giuseppe, G., Boscaro, V., and Keeling, P.J. (2016). Biogeography and character evolution of the ciliate genus euplotes (Spirotrichea, euplotia), with description of euplotes curdsi sp. nov. PLoS ONE *11*, e0165442.

106. Valbonesi, A., and Luporini, P. (1990). A new marine species of euplotes (ciliophora, hypotrichida) from antarctica. Bull. Br. Museum Natl. Hist. Zool. *56*, 57–61.

STAR★METHODS

KEY RESOURCES TABLE

REAGENT or RESOURCE	SOURCE	IDENTIFIER
Chemicals, peptides, and recombinant proteins		
Protozoa pellets	Blades Biological Ltd	Cat# CBA053
HEPES	Sigma-Aldrich	Cat# H3375-250G
HEPPS	Sigma-Aldrich	Cat# E9502-100G
BSA	Sigma-Aldrich	Cat# A9418-100G
EGTA	Sigma-Aldrich	Cat# E3889-25G
Tween-20	Sigma-Aldrich	Cat# P1379-25ML
TRIS-base	Fisher Bioreagents	Cat# BP152-1
DAPI	ThermoFisher	Cat# D1306
NaCl	Sigma-Aldrich	Cat# 31434-1KG-M
KCl	Fisher Chemical	Cat# P/4280/53
CaCl2	Fisher Chemical	Cat# C/1500/53
MgCl2	Fisher Bioreagents	Cat# BP214-500
Critical commercial assays		
DNeasy Plant Pro kit	Qiagen	Cat#69204
Deposited data		
Electrophysiology recordings	This study	Zenodo: https://doi.org/10.5281/zenodo.10391984
Waveforms	This study	Zenodo: https://doi.org/10.5281/zenodo.10391984
Trajectory data	This study	Zenodo: https://doi.org/10.5281/zenodo.10391984
Experimental models: Organisms/strains		
Euplotes vannus	This study. Deposited at www.ccap.ac.uk.	CCAP 1624/35 Euplotes vannus
Software and algorithms		
Fiji	J. Schindelin et al.[99]	https://imagej.net/software/fiji/; RRID:SCR_002285
TrackMate	J.-Y. Tinevez et al.[100]	https://imagej.net/plugins/trackmate/
Micro-Manager	A. Edelstein et al.[101]	https://micro-manager.org; RRID:SCR_016865
MATLAB	Mathworks	https://uk.mathworks.com/; RRID:SCR_001622
Wavesurfer	HHMI Janelia Research Campus	https://wavesurfer.janelia.org/
SLEAP	T. D. Pereira et al.[73]	https://sleap.ai/; RRID:SCR_021382
BLASTn suite	NCBI	https://blast.ncbi.nlm.nih.gov/Blast.cgi; RRID:SCR_001598
DADA2	B. J. Callahan et al.[102]	https://benjjneb.github.io/dada2/; RRID:SCR_023519
Bioelectric states and motility states classification	This study	Zenodo: https://doi.org/10.5281/zenodo.10391984

RESOURCE AVAILABILITY

Lead contact

Further information and requests for resources and reagents should be directed to and will be fulfilled by the lead contact, Kirsty Wan (k.y.wan2@exeter.ac.uk).

Materials availability

The *Euplotes vannus* culture established as part of this study has been deposited at the Culture Collection of Algae and Protozoa (CCAP) and has been allocated the CCAP accession number: CCAP 1624/35 Euplotes vannus.

Data and code availability

Membrane potential recordings, waveform data, and trajectory data have been deposited at Zenodo. DOIs are listed in the key resources table. All other data, including the video recordings, acquired as part of this study will be shared by the lead contact upon request.

Original code has been deposited at Zenodo and is publicly available as of the date of publication. DOIs are listed in the key resources table.

Any additional information required to reanalyze the data reported in this paper is available from the lead contact upon request.

EXPERIMENTAL MODEL AND SUBJECT DETAILS

Cell culturing

The *Euplotes* species used in this study was identified and isolated from cultures of coral larvae received from the Horniman Museum Aquarium in London during December 2020 and January 2021. 18S sequencing confirmed the genus to be *Euplotes*, and based on BLAST analysis results combined with morphological comparisons we conclude that the species is *Euplotes vannus* (see *Species classification* section below and Table S1 for details).

Cultures were maintained under low light conditions (approximately 1-19 lux measured with a RS-8809A light meter, RS-Pro) at 21°C, and were sub-cultured every 2-4 weeks in media prepared by dissolving protozoan pellets (CBA053, Blades Biological Ltd) in artificial seawater at half the recommended concentration (i.e. 1 pellet in 2L).

Species classification

18S sequencing and analysis

Culture samples were washed 5 times in filter sterilised (0.2 μm syringe filter) artificial seawater and harvested by centrifugation at 2000-3166 rcf. DNA was then extracted using a DNeasy Plant Pro kit (Qiagen) and sent for 18S amplicon sequencing at the Exeter Sequencing Service, University of Exeter. 18S DNA was amplified by Polymerase Chain Reaction between the primer annealing sites 5'-GTACACACCGCCCGTC-3' (18S_Euk_1391f) and 5'-TGATCCTTCTGCAGGTTCACCTAC-3' (18S_EukBr) using a modified Illumina protocol for the generation of amplicon libraries using a 2 step PCR[103] and unique dual indexing. The purified amplicon libraries were denatured and diluted to 0.5 nM and 150 paired-end sequenced on the NovaSeq 6000 using v1.5 SBS reagents (Illumina Inc. USA) with other samples according to the manufacturers protocol. After sequencing, the data was run through a DADA2 pipeline[102] including removal of primers, filtering low quality reads, denoising, merging paired ends and chimera removal. The number of reads lost at each stage was minimal, suggesting the libraries and sequencing are of good quality. This process identified 36 18S sequences, illustrating that the culture is a microbial consortium. The vast number of reads correspond to the five most frequently occurring sequences (i.e. the highest five no. of reads were 47255, 3952, 811, 110 and 60). BLASTn analysis of the most abundant sequence hits 125 full length sequences with 100% identity match and covering different *Euplotes* and *Moneuplotes* species (see Table S1), note that *Moneuplotes* has a homotypic synonym *Euplotes*. Overall, this 18S sequence analysis confirms that the organism is from the genus *Euplotes* and provides a shortlist of potential classifications to the species level (Table S1).

Morphological comparisons

To confirm the identity of the *Euplotes* species used in this work, we next turn to morphological characteristics of the cell revealed by brightfield imaging, confocal microscopy and SEM (Figure 1 and Figure S1). The *Euplotes* species used in this study has 10 fronto-ventral cirri and 5 transverse cirri, typically 4 caudal cirri, a single type dorsal argyrome, a C-like shaped macronucleus with a twisted extension and a micronucleus at the anterior end often very close to the macronucleus. Additionally, the cell body is approximately 72-92μm long and 34-43μm wide and 15-22μm high (measured from bright-field images, N = 14, 8 and 6 respectively). Comparing these morphological characteristics with those described in the references[104–106], they were found to be most consistent with *Euplotes vannus* (see Table S1; Figure S1). Overall, we conclude that the species used in this study is *Euplotes vannus*.

METHOD DETAILS

Scanning electron microscopy

For ultrastructural investigation, *Euplotes vannus* culture samples were concentrated by centrifugation at 1000g for 20 mins followed by removal of supernatant to achieve a 4-fold concentration. Cells were then fixed in 2% paraformaldehyde and 2% glutaraldehyde in 0.1M sodium cacodylate containing sea water, pH 7.2 for 2 h at room temperature. To help with sample processing, cells were kept in small baskets, prepared from 1.5 ml centrifuge tubes. The basket was then created by applying a small rectangular piece of 30 μm nylon mesh, large enough to cover the tube diameter, which was sealed with the lid of the prepared centrifuge tube. Turned upside down, this creates a small basket which can be easily transferred into glass vials containing the various sample preparation solutions. After 3 x 5 min washes in buffer, the samples were post-fixed in 1% osmium tetroxide in deionized water for 1 h at room temperature. Following 3 x 5 min washes in deionized water, cells were dehydrated in a graded ethanol series (30, 50, 70, 80, 90, 95% - 5 min per step, followed by 2 x 10 min in 100% ethanol) and subsequently incubated for 3 min in HMDS (Hexamethyldisilazane, Merck, Gillingham, UK) and air drying. Fully dried samples were mounted on aluminium stubs with the help of carbon tabs and coated with 10 nm gold-palladium (80/20) in a sputter coater (Q150T, Quorum, Lewes, UK) before imaging in a scanning electron microscope (Zeiss Gemini 500 SEM) operated at 1.5 kV and a SE2 detector.

DAPI staining and confocal imaging

Euplotes vannus culture samples were first concentrated approximately 5-fold by centrifugation at 1000g for 10 minutes. Cells were then permeabilised in PHEM buffer (60 mM PIPES, 25 mM HEPES, 10 mM EGTA, 2 mM MgCl$_2$, pH 6.9) containing 1% Triton X-100

for 2 minutes, after which the cells were fixed for 10 minutes by adding paraformaldehyde (2% final concentration). The cells were then washed twice by centrifugation at 1000g for 5 minutes and resuspension in TBST/BSA (10 mM Tris, 0.15M NaCl, pH 7.4, containing 0.1% Tween-20 and 3% BSA). After staining the nuclei with DAPI (1 μg ml^{-1}) for 5-10 minutes at room temperature, cells were washed twice by centrifugation at 1000g for 5 minutes and resuspension in TBE (10 mM Tris, 0.15 M NaCl). Images were acquired using a confocal laser scanning microscope (Zeiss LSM 880 with Airyscan Fast).

Experimental solutions

The medium used for behavioural observations and electrophysiological experiments was EASW (Artificial Sea-Water for Electrophysiology), which contained 430 mM NaCl, 10 mM KCl, 10 mM CaCl$_2$, 53 mM MgCl$_2$ and 10 mM HEPPS; pH 8.0-8.1. Cells were transferred from the growth medium by centrifuging at 1000 g for 5 mins then re-suspending in EASW three times. For electrophysiology experiments the cells were concentrated 2-fold during the final re-suspension.

Imaging and tracking the behaviour of freely moving cells

The free swimming and walking trajectories of *Euplotes vannus* were recorded at $40 - 53$ fps using a pco.panda 4.2 M camera mounted on a Leica M205 C stereomicroscope, with 2× magnification. Cells were free to roam in a $700 - 800$ ml volume. Trajectories were obtained using TrackMate in Fiji.[100] Motility trajectories were manually classified according to walking or swimming, and further analysis of swimming speed and walking behaviours were performed using custom MATLAB scripts (see *Trajectory analysis* section below). To capture the cirri dynamics of freely walking cells, videos were recorded at 800 fps using a Phantom v1212 camera mounted on a Leica DMi8 inverted microscope with 40× and 20× objectives, in brightfield. To ensure that all images and trajectories are consistent with a bottom-up view of the cells (i.e. viewing from below), the images and trajectories were reflected, and care was taken to preserve this consistency when transferring TrackMate results into MATLAB.

Trajectory analysis

Digital trajectories consisted of 2D coordinates (x, y), at discrete times (t). The cell speed is defined as $v = \sqrt{\Delta x^2 + \Delta y^2}/\Delta t$, here calculated after smoothing using a 2nd order Savitzky-Golay filter. We use the four-quadrant inverse tangent to define a track angle $\omega = \text{atan } 2(|\boldsymbol{p} \times \boldsymbol{q}|, \boldsymbol{p} \cdot \boldsymbol{q})$, from vectors $\boldsymbol{p}$ and $\boldsymbol{q}$, approximately tangential to the track at adjacent times (Figure S2). Positive ω corresponds to a counter-clockwise angle.

We also obtain an ellipse angle θ (also from TrackMate), defined as the angle of the major axis of the fitted ellipse with respect to the x-axis of the image (Figure S2), with a positive value indicating that the ellipse angle is increasing (i.e. here turning counter-clockwise for a bottom-up view). For the states assignment we apply a smoothing filter to θ, and work with $\Theta = |\Delta \cos 2\theta /\Delta t|$.

Assignment of motility states

Trajectories of walking cells are discretised into 3 motility states: stop ($i_{\text{state}} = 0$), forwards walking ($i_{\text{state}} = 1$) and SSR events ($i_{\text{state}} = 2$); see Figure 1G and Figure S2. To distinguish between 'stop' ($i_{\text{state}} = 0$) and 'moving' ($i_{\text{state}} \in [1, 2]$) states, a speed threshold of 60 μm s^{-1} is applied to the moving mean of speed v (window width of 10 frames). SSR events ($i_{\text{state}} = 2$) are identified using peaks in the ellipse angle parameter Θ, corresponding to large changes in cell orientation, and the track angle ω is used to define the start and end times of each SSR event. An SSR event typically consists of a double peak in the track angle magnitude $|\omega|$, the first and primary peak corresponding to the initiation of the backwards motion of the cell and the later secondary peak to the cell turning. The start of an SSR is defined to be the location of the primary peak (located before the corresponding peak in Θ). The end of an SSR is defined based on either the location of the secondary peak in $|\omega|$, or the location of the peak in Θ, whichever is later. Thus, $t_{\text{end}} = t_{\text{pk}} + w/2$, where t_{pk} is the time point of the chosen later peak and w its width at half maximum. Any SSR events with a mean speed <100μm s^{-1} are false-positives and reclassified as forwards walking ($i_{\text{state}} = 1$).

SSR characteristics

We define a set of parameters to characterise the SSR (Figure S2). As well as the duration T_{SSR}, we define a turning angle $\alpha = -(\pi - |\omega_{\text{pk}}|)\omega_{\text{pk}}/|\omega_{\text{pk}}|$, where ω_{pk} is the track angle corresponding to the secondary peak identified in $|\omega|$. This gives $-\pi \leq \alpha \leq \pi$, with positive α corresponding to a counter-clockwise turn.

Distribution fits

Probability density functions (pdf) were fit with either a gaussian distribution pdf $= \frac{1}{\sigma\sqrt{2\pi}} \exp\left(-\frac{(x-\mu)^2}{2\sigma^2}\right)$, or an exponential distribution pdf $= \frac{1}{\mu} \exp(-x/\mu)$, where μ is the mean and σ the standard deviation.

Electrophysiology and high-speed imaging

Intracellular recording electrodes were made from filamented borosilicate glass capillaries with inner and outer diameters of 1 and 0.5 mm respectively (GBF-100-50-10, WPI). Electrodes with a $0.9 - 0.5$μm tip were pulled using a P-1000 Puller (Sutter Instrument), filled with 1 M KCl and had resistances of $\sim 60 - 100$ MΩ. The electrode was mounted onto a HS-9-0.1x headstage connected to an Axoclamp 900A amplifier (Molecular Devices), which was connected to the computer with a PCIe-6341, X Series DAQ board (National Instruments) and operated using the Axoclamp 900A commander software. After enabling the bridge balance

and zeroing the voltage reading in the EASW bath solution, the electrode was inserted into a cell held fixed with a suction micropipette pulled from TW-120 borosilicate glass capillaries (WPI) using a P-1000 Puller (Sutter Instruments). Micropipettes were scored and broken off to give an o.d. $\sim 60 - 70$ μm and fire polished to create a rounded tip with i.d. $\sim 10 - 25$ μm. Electrophysiological recordings were acquired using the WaveSurfer software, a MATLAB-based platform (https://wavesurfer.janelia.org/), while videos were acquired at $130 - 250$ fps using a PRIME 95B camera (Photometrics) mounted on a Nikon Ti2-U Eclipse microscope and controlled using Micro-Manager.[101] In order to synchronise the electrophysiological recordings and video acquisition, the stimulus package in WaveSurfer was used to send a trigger signal to the camera via the PCIe-6341, X Series DAQ board (National Instruments).

Analysis of membrane depolarisation events

Custom MATLAB scripts were used to identify and analyse membrane depolarisation events. First, the signal is detrended using a 2nd order polynomial to obtain the detrended membrane potential $V(t)$. Second, a multi-modal gaussian is fit to the distribution of $V(t)$ using pdf $= \sum_{n=1}^{N_{\text{gauss}}} A_n \frac{1}{\sigma_n \sqrt{2\pi}} \exp\left(- \frac{(x-\mu_n)^2}{2\sigma_n^2}\right)$, where the number of gaussians N_{gauss} is determined by the number of peaks in the distribution, and μ_n, σ_n and A_n are the mean, standard deviation and coefficient respectively for the nth gaussian. Third, a voltage threshold is defined as $V_c = \mu_{\text{pk}} + \sigma_{\text{pk}} + 1.5$, where μ_{pk} and σ_{pk} are the mean and standard deviation respectively for the gaussian fit with the largest value of A_n for $-40 < \mu_n < -10$ mV. Finally, the bioelectric activity is discretised into two states (baseline = 0 and depolarisation events = 1) by applying the voltage threshold V_c to the moving mean of $V(t)$ (window width 0.25 s). Any instances where the maximum in the moving mean of $V(t)$ during the depolarisation is $< V_c + 1$ mV are removed and reassigned to the baseline state.

We define the depolarisation transition from state 0 to 1 as a step-up, and the subsequent repolarisation from state 1 to 0 as a step-down response. To superimpose the depolarisation and repolarisation phases, the time series are centred at t_i, the time point at which the membrane potential crosses the V_c threshold. For each depolarisation we define the relative membrane potential V_{rel} by subtracting the mean membrane potential 0.5-1 s *before* t_i. Similarly, for each repolarisation we define the relative membrane potential V_{rel} by subtracting the mean membrane potential 0.5-1 s *after* t_i. The size of the step $\Delta V = V_{\text{max}} - V_{\text{min}}$, where V_{max} and V_{min} are the maximum and minimum values respectively for the moving mean of $V(t)$ (window width 0.25 s) within $t_i \pm 0.5$ s. The rate dV/dt is calculated using the moving mean of $V(t)$ with window width 0.125 s. The results for dV/dt are reported here as the moving mean with window width 0.25 s. The peak in dV/dt associated with each depolarisation and repolaristaion is defined as the maximum $|dV/dt|$ within $t_i \pm 0.5$ s.

Cirri frequency analysis

We first apply a median filter to the videos, then manually defined (using Fiji[99]) rectangular regions of interest (ROI) and measured the mean intensity I_{ROI} within this region. Further analysis of I_{ROI} was performed using custom MATLAB scripts. The chosen ROI specifies an area passed through by a specific cirrus and oscillates in accordance with the beat period. The time-resolved cirrus frequency is given by $f(t) = 1/T(t)$, where $T(t)$ corresponds to the beat period calculated as the time between neighbouring peaks in $-I_{\text{ROI}}$ (Figure 2C). Note that due to the presence of multiple cirri with overlapping waveforms, sometimes other cirri pass through the ROI. Therefore, $f(t)$ is correlated with cirri activity but is not always a direct measure of the cirri beat frequency. A normalised frequency is defined as

$$\bar{f}(t) = \frac{f(t) - f_{\text{min}}}{f_{\text{max}} - f_{\text{min}}}, \qquad \text{(Equation 6)}$$

where f_{min} and f_{max} are the minimum and maximum values of $f(t)$ respectively.

Cross-correlations

The cross-correlation of two time-series $x(t)$ and $y(t)$ as a function of the time-lag τ is given by

$$r_{x,y}(\tau) = \frac{\sum_t (x(t) - \mu_x)(y(t+\tau) - \mu_y)}{\sqrt{\sum_t (x(t) - \mu_x)^2 \sum_t (y(t) - \mu_y)^2}}, \qquad \text{(Equation 7)}$$

where μ_x and μ_x are the mean of $x(t)$ and $y(t)$ respectively. Cross-correlations were computed using custom MATLAB scripts.

Tracking cirri using SLEAP

The machine learning tool SLEAP[73] was used to obtain tracks of the cirri shape by using a multi-animal model such that each cirrus was considered an 'animal' and using a skeleton of 4 nodes connected in a line (see Figure 3A). The model was trained on 51 frames ($\sim 10\%$ of the entire video). Post-processing of the cirri tracks was required in-order to improve the results. First, the position of node 1 was used to obtain a more effective labelling of the cirri identities based on threshold values of the x-position of node 1: $x_{1,1} < 160$ pixels and $200 \leq x_{2,1} < 250$ pixels, where $x_{i,1}$ is the x coordinate of node 1 for cirrus i. Second, missing nodes were linearly interpolated.

Probability flux of SLEAP-tracked cirri tips

Cirri tip trajectories were defined as $\boldsymbol{x}_{tip,i} = \boldsymbol{x}_{i,4} - \boldsymbol{x}_{i,1}$, where $\boldsymbol{x}_{i,4}$ is the position of the cirrus tip (node 4) and $\boldsymbol{x}_{i,1}$ the position of the cirrus base (node 1), for cirrus i. The probability flux for cirri tip trajectories was calculated using the method described in Bentley et al.[20] Briefly, the 2D positional space is divided into a grid of equally sized square boxes side length Δx. From a trajectory, a time-series of box transitions is obtained, giving the transition matrix

$$A = \begin{bmatrix} (i,j)_1 & (i,j)_2 & t_{1,2} \\ (i,j)_2 & (i,j)_3 & t_{2,3} \\ \dots & \dots & \dots \\ (i,j)_{N-1} & (i,j)_N & t_{N-1,N} \end{bmatrix}, \quad \text{(Equation 8)}$$

where $(i,j)_n$ and $(i,j)_{n+1}$ are the positions of consecutively visited boxes and $t_{n,n+1}$ is the time spent in the initial state $(i,j)_n$ prior to the transition. When two successive states $(i,j)_n$ and $(i,j)_{n+1}$ do not correspond to nearest neighbours, the intermediate boxes are determined by linear interpolation and the extra transitions are inserted into the array A (Equation 8). Note that this calculation did not account for diagonal transitions, which are assumed to be negligible. For a trajectory of total duration t_{total}, the net transition rate between neighbouring boxes is given by

$$\omega_{(i,j)(k,l)} = \frac{1}{t_{total}} \left(N_{(i,j)(k,l)} - N_{(k,l)(i,j)} \right), \quad \text{(Equation 9)}$$

where $N_{(i,j)(k,l)}$ is the number of transitions from box (i,j) to box (k,l). The probability flux is then calculated according to

$$\boldsymbol{j}_{(i,j)} = \frac{1}{2\Delta x} \left(\begin{array}{c} \omega_{(i,j)(i+1,j)} + \omega_{(i-1,j)(i,j)} \\ \omega_{(i,j)(i,j+1)} + \omega_{(i,j-1)(i,j)} \end{array} \right). \quad \text{(Equation 10)}$$

The 2D trajectories of the tip were also used to calculate the probability density function, $\text{pdf} = n_{i,j}/(NA_{box})$, where $n_{i,j}$ is the number of trajectory points in box (i,j), N the total number of trajectory points and $A_{box} = \Delta x^2$ the box area.

Cirri beat characteristics for SLEAP-tracked cirri

Beat frequency was determined using the tip-to-base distance $d = |\boldsymbol{x}_{i,4} - \boldsymbol{x}_{i,1}|$, i.e. the distance between node 1 and node 4 for the SLEAP-tracked cirri. Peaks in $-d$ were used to give the beat period T, with instantaneous beat frequency given by $f = 1/T$. The beat amplitude D is defined as the mean value of d for each cycle. A moving mean was used to reduce noise. The cross-correlation was calculated for all pairs of the three variables $f(t)$, $D(t)$ and $V(t)$.

RFT and model calculations

Cirri waveforms were hand traced using Fiji, with subsequent spline fitting and force calculations implemented in Python. Traces were interpolated using a cubic fitting to increase the sampling frequency 4-fold and achieve a $\Delta t = 0.0012$ s. The power stroke phase was defined as periods during which $F_x > 0$, $F_y > 0$ and $F_x < -10$ pN for the Type I, Type II and Type III waveforms respectively. Using these power stroke assignments, the average forces $\langle \boldsymbol{F}_{PS} \rangle = 1/\tau_{PS} \int_{t_{PS}} \boldsymbol{F}(t)dt$ and $\langle \boldsymbol{F}_{RS} \rangle = 1/\tau_{RS} \int_{t_{RS}} \boldsymbol{F}(t)dt$, and torques $\langle \boldsymbol{T}_{PS} \rangle = 1/\tau_{PS} \int_{t_{PS}} \boldsymbol{T}(t)dt$ and $\langle \boldsymbol{T}_{RS} \rangle = 1/\tau_{RS} \int_{t_{RS}} \boldsymbol{T}(t)dt$ were obtained for the power stroke (PS) and recovery stroke (RS) phases respectively, where τ_{PS} and τ_{RS} are the estimated duration of the power and recovery stroke phases.

The cell's speed and angular velocity was tracked from high-speed video using TrackMate, again defining $\boldsymbol{x}$ and ellipse angle θ. The speed of each segment is given by $\boldsymbol{v} = \Delta \boldsymbol{x}/\Delta t$. An unit orientation vector $\hat{\boldsymbol{o}}$ is defined as the orientation of the long axis of the fitted ellipse, as obtained from TrackMate. The speed in the x-direction of the cell is then given by $v_x = \boldsymbol{v} \cdot \hat{\boldsymbol{o}}$. The angular velocity is defined as $\Omega = \Delta \theta / \Delta t$.

Manual annotation of cirri activity

When the cell is walking forwards (i.e. $t = 0.5 - 0.85$ s), the 10 frontoventral cirri (a-j) are seen to be performing the Type I waveform and were manually assigned to either the power stroke (PS) or recovery stroke (RS) in each frame. During an SSR event (i.e. $t = 2 - 2.4$ s), the 10 frontoventral cirri (a-j) perform the Type II waveform starting at $t \sim 2.08$ s, whereas the 5 transverse cirri (k-o) perform the Type III waveform starting at $t \sim 2.04$ s. The cirri were again assigned to either the power stroke (PS) or recovery stroke (RS) phase of the corresponding waveform. For each of the three waveforms, a period of the video is identified which approximately corresponds to one beat cycle, i.e. $t_I = 0.52 - 0.66$ s, $t_{II} = 2.12 - 2.21$ s and $t_{III} = 2.07 - 2.19$ s for the Type I, II and III waveforms respectively. The average speed $\langle v_x \rangle = 1/\tau_i \int_{t_i} v_x(t)dt$ and average angular velocity $\langle \Omega \rangle = 1/\tau_i \int_{t_i} \Omega(t)dt$ were calculated, where i indicates the waveform type and τ_i is the total duration of the period t_i. Similarly, the time series of the cirri power and recovery stroke assignments are used to obtain the time-averaged number of cirri performing the power stroke, $\langle N_{PS,i} \rangle = 1/\tau_i \int_{t_i} N_{PS,i}(t)dt$, for each of the waveforms Type $i = $ I, II and III.

As described in the main text, N_{PS} was estimated using our minimal model by imposing force free and torque free conditions, where $\boldsymbol{F}_{cirri} = \boldsymbol{F}_I + \boldsymbol{F}_{II} + \boldsymbol{F}_{III}$, where $\boldsymbol{F}_i$ is the force associated with the Type i waveform and is given by $\boldsymbol{F}_i = N_{PS,i} \langle \boldsymbol{F}_{PS,i} \rangle + N_{RS,i} \langle \boldsymbol{F}_{RS,i} \rangle$, where $\langle \boldsymbol{F}_{PS,i} \rangle$ and $\langle \boldsymbol{F}_{RS,i} \rangle$ are the time-averaged forces for the Type i waveform estimated from RFT calculations. Similarly $\boldsymbol{T}_{cirri} = \boldsymbol{T}_I + \boldsymbol{T}_{II} + \boldsymbol{T}_{III}$, with the torque for the Type i waveform estimated as $\boldsymbol{T}_i = N_{PS,i} \langle \boldsymbol{T}_{PS,i} \rangle + N_{RS,i} \langle \boldsymbol{T}_{RS,i} \rangle$. For the Type I and II waveforms $N_{RS} = 10 - N_{PS}$, while for the Type III waveform $N_{RS} = 5 - N_{PS}$.

QUANTIFICATION AND STATISTICAL ANALYSIS

Statistical details (including the value of n, what n represents and the definition of precision measurements) of the experiments can be found in the main text, figure legends, table legends or method details section. Precision measurements are given as the mean and standard deviation, unless otherwise stated.